We are IntechOpen,
the world's leading publisher of
Open Access books
Built by scientists, for scientists

7,000
Open access books available

186,000
International authors and editors

200M
Downloads

154
Countries delivered to

Our authors are among the

TOP 1%
most cited scientists

12.2%
Contributors from top 500 universities

CLARIVATE ANALYTICS
BOOK CITATION INDEX
INDEXED

WEB OF SCIENCE™

Selection of our books indexed in the Book Citation Index
in Web of Science™ Core Collection (BKCI)

Interested in publishing with us?
Contact book.department@intechopen.com

Numbers displayed above are based on latest data collected.
For more information visit www.intechopen.com

Diode Pumped Planar Waveguide/Thin Slab Solid-State Lasers

Jianqiu Xu

*Key Laboratory for Laser Plasmas (Ministry of Education) and
Department of Physics, Shanghai Jiaotong University, Shanghai
China*

1. Introduction

Diode-pumped solid-state lasers (DPSSLs) with high power and good output beam quality are widely used in material processing, communication, remote sensing, and medical treatment. A preferable diode-pumped solid-state laser has the characteristics, such as high efficiency, long lifetime, high reliability, compact size and flexibility. Planar waveguide lasers can be formed by transition metal diffusion method, optical bonding technique, or ion-etching technique. Planar waveguides used for high-power lasers are usually the simplest one-dimensional waveguides, of which the width (the dimension along the y-direction) is much large than the laser wavelength. The laser beam is guided only in the x-direction as shown in Fig. 1.1. The behavior of beam along the y-direction is similar as the beam propagating in the free space. We consider a planar isotropic optical waveguide, where the active core $x<\pm d/2$ is occupied by the homogeneous gain medium, and the claddings $x>\pm d/2$ consist of the semi-infinite substrate. The z-axis is taken in the direction of beam propagation. The refractive index of core and cladding are n_0 and n_1, respectively.
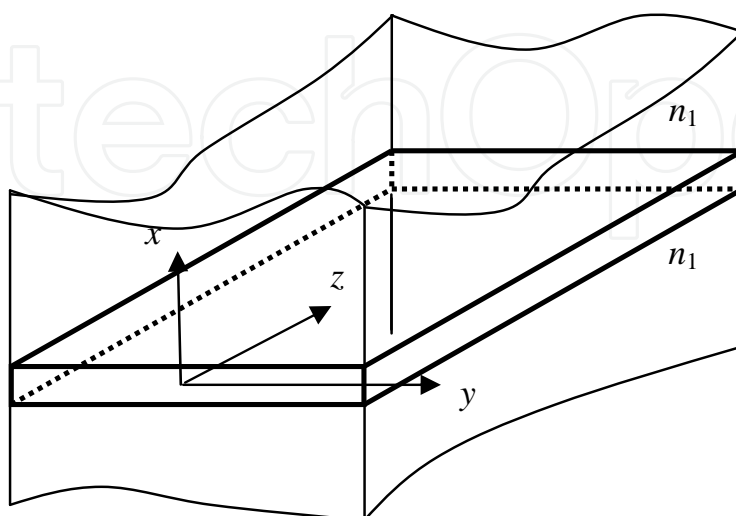

Fig. 1.1. Structure of planar optical waveguide.

Usually, the aspect ratio of the planar waveguide/thin slab lasers is very large. The dimension in the width direction is much larger than beam widths of fundamental modes of stable resonators, and the diffraction-limited beam from a stable resonator is difficult to be achieved. The unstable resonator, with large fundamental mode volume and much higher-order mode discriminations, has been employed successfully in the planar waveguide gas lasers. Unlike gas lasers, thermal distortion and pumping non-uniformity in solid-state lasers are serious limitations for achieving good beam quality in using unstable resonators. These distortion and non-uniformity should be considered in the design of unstable resonators.

1.1 Pump uniformity for planar waveguide lasers

The pump uniformity for planar waveguide lasers is discussed for the absorption of pump power in the active waveguide. Using special composite waveguide design and controlling the incident angle of the pump light would reduce the pump non-uniformity. A typical configuration of planar waveguide lasers pumped by laser diodes from double edges is shown in Fig. 1.2(a). To achieve large beam diameters along the width direction, off-axis unstable resonator is applied. The resonator is constructed by a high reflective mirror and a hard-edge output coupler. Both are concave mirrors. Although negative branch confocal unstable resonator is dispatched in the figure, positive branch confocal unstable resonators can also be used. In the thickness direction the beam characteristics are determined by the waveguide structure, and in the width direction the beam quality is controlled by the cavity design. Because the beam propagation in these two directions is independent [1], we can concentrate our investigations on the width direction.
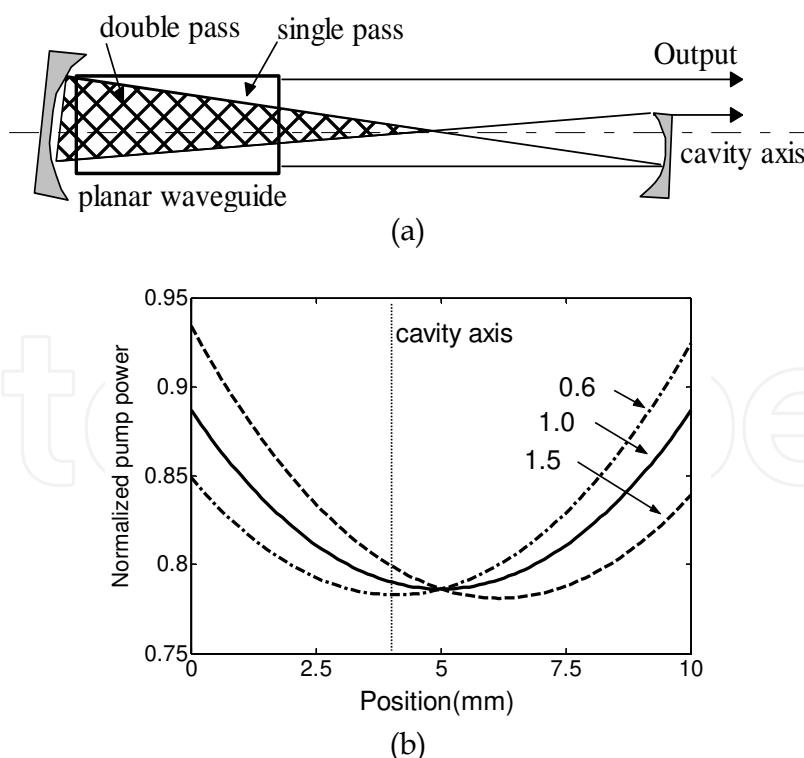

(a)

(b)

Fig. 1.2. (a) Edge pumped planar waveguide lasers with negative branch confocal unstable resonator. (b) Normalized pump power along the width direction of the planar waveguide for asymmetric factors b = 0.6, 1.0, and 1.5. The absorption coefficient α = 0.3 cm^{-1}.

Because of absorption of pump power in the active waveguide, the pumping distribution along the width direction is non-uniform as shown in Fig. 1.2(b). If identical laser diodes are used on the two sides, a minimum of the pumping density is located at the center of the waveguide [2]. Notice that only a part of the crystal waveguide is double-pass covered by the laser beam in the resonator. The effective fill-factor is defined as [1]

$$F_{eff} = \frac{\iint_{S+} P_{abs}(x,z) \; dxdz + \iint_{S-} P_{abs}(x,z) \; dxdz}{2\iint_{S0} P_{abs}(x,z) \; dxdz} \tag{1.1}$$

where S_0 is area of the crystal waveguide, S_+ and S_- are the area covered by the forward (from left hand side to right hand side in the Fig. 1.2a) and the backward laser beam, respectively. Obviously $S_+ \neq S_-$. Clearly, a unit effective fill-factor means full covering of the laser beam on the waveguide. The distribution of pumping density is calculated by

$$P(x) = C_0 \left\{ \cosh[\frac{\alpha w}{2} - \ln\sqrt{b} - \alpha x] + Re^{-\alpha w} \cosh[\frac{\alpha w}{2} + \ln\sqrt{b} - \alpha x] \right\} \tag{1.2}$$

with the normalized coefficient

$$C_0 = \frac{P_{in}}{tl} \frac{2(1-R)\sqrt{b}e^{-\frac{\alpha w}{2}}}{(1+b)(1-R^2 e^{-2\alpha w})} \tag{1.3}$$

where α is the absorption coefficient of the active medium; P is launched power from LD in the upper side (Watt/cm); t, l and w are the thickness, length and width of the planar waveguide, respectively; R is the reflectivity of side surface; b is the pumping asymmetric factor, defined by the pump power ratio of down to upper sides as shown in Fig. 1.2(a). The pumping minimum offsets roughly by $\ln\sqrt{b} / \alpha$ from the center with a symmetric factor of b. By choice of different laser diodes in the down and upper sides, we can adjust the asymmetric factor so that the pumping distribution overlaps mostly with the laser beam, and consequently the pumping efficiency is increased. Figure 1.3(a) shows the calculated effective fill-factors for various asymmetrical pumping. The parameters used in the calculations are described in Table 1.1. Fill-factors reach larger values with larger asymmetric pumping. Since high absorption coefficients give rise to large pumping non-uniformities, improvement of fill-factor by asymmetric pumping is more efficient for heavy doping concentration. Lower doping concentration and smaller absorption coefficients give higher fill-factors, but wide waveguide is required to achieve high pump absorption efficiency. An optimum doping concentration is a trade-off of these effects. Because the beam converges more hard in the short cavity, the effective fill-factor is enlarged with increasing cavity length (see Fig. 1.3b).

Radius of curvature rear mirror	Radius of curvature front mirror	Waveguide dimension	Cavity length	Cavity magnification
285.6	200	55(l)×10(w)	242.8	1.428

Table 1.1. Cavity and waveguide parameters (mm)

High efficient absorption and perfectly uniform pumping are very difficult to be achieved simultaneously in the edge-pumped slab lasers, and the pump intensities near edges are always higher than that at the center of slab. The difference between the maximum and minimum pump intensity can be written as a function of the pump absorption efficiency η_{abs} in the form [1]

$$\Delta I = \frac{I_{max-min}}{I_{max}} = 1 - \frac{2\sqrt{1-\eta_{abs}}}{2-\eta_{abs}} \tag{1.4}$$
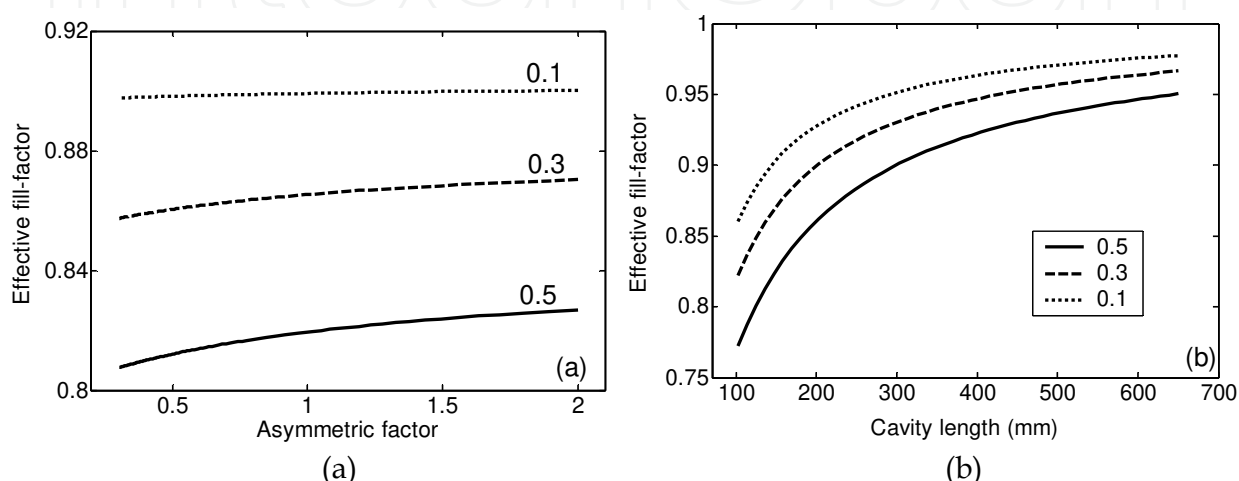

Fig. 1.3. (a) Effective fill-factor with varying asymmetric factor. (b) Effective fill-factor vs. cavity length with symmetric pumping for absorption coefficient α=0.1, 0.3 and 0.5 cm^{-1}.

The more the pump power is absorbed, the higher the pump non-uniformity occurs. The figure of merit of pump performance is defined as [5],

$$F = \Delta I + \frac{2\sqrt{1-\eta_{abs}}}{2-\eta_{abs}} \tag{1.5}$$

where F=1 for the traditional edge-pumped slab lasers, and F=0 for the case with total absorption and perfect uniformity.

The pump non-uniformity comes mainly from the preferential absorption near the edge. We can control the incident angle of the pump light entering the waveguide to prevent a part of them from being absorbed near the edge, or use special composite waveguide design to improve the pump intensity near the center. The ideals using composite waveguide and oblique pumping are illustrated in Fig. 1.4. The composite YAG/Yb:YAG slab crystal was taken for example. The total width of the slab is 1 mm and the doping section is in the center of the slab with the Yb^{3+}-ion doping concentration of 4 at.%, and its thickness is 0.4 mm.

The method of ray tracing was used to simulate the pump behavior in the waveguide. In figure 1.4, the waveguide with plane cladding and concave cladding is irradiated by the LD at an inclination angle. In our simulation, the pump power of each LD was 100 W. The

pump light with the beam divergence angle of $b=7.5°$ enters the waveguide at the inclination angle of $a=5°$.

Figure 1.4(a) described the pump intensity *versus* width of waveguide with the plane cladding. It was seen that the ratio between the maximum and the minimum intensity of the plane slab is $\Delta I=33.3\%$ and the absorption efficiency is $\eta_{abs}=90\%$. The figure of merit is $F=0.9$ which is better than the result when the absorption $\eta_{abs}=90\%$ is inserted into Eq. (1.4). To make further improvement, the upper cladding is made to a concave profile as shown in Fig. 1.4. (a). Figure 1.4(b) depicted the pump intensity through the width of the concave slab. The difference between the maximum and minimum intensity is $\Delta I=10.8\%$, corresponding the figure of merit $F=0.68$, which is in the same level as that in face pumped solid-state slab lasers.
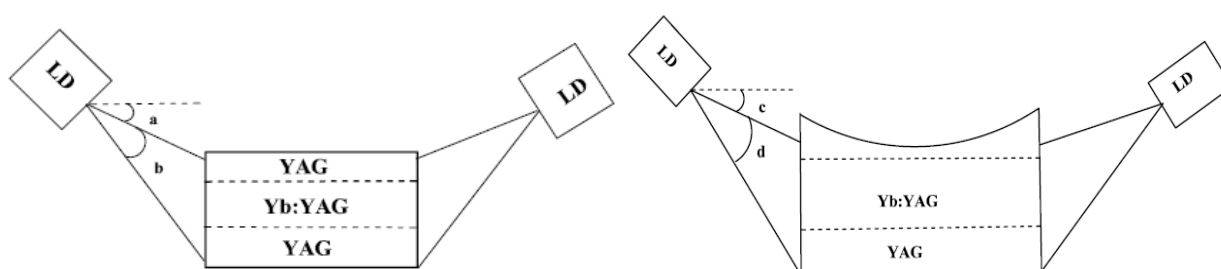

Fig. 1.4. (a). Schematic diagram of edge-pumped slab laser with plane cladding (left), concave cladding (right).
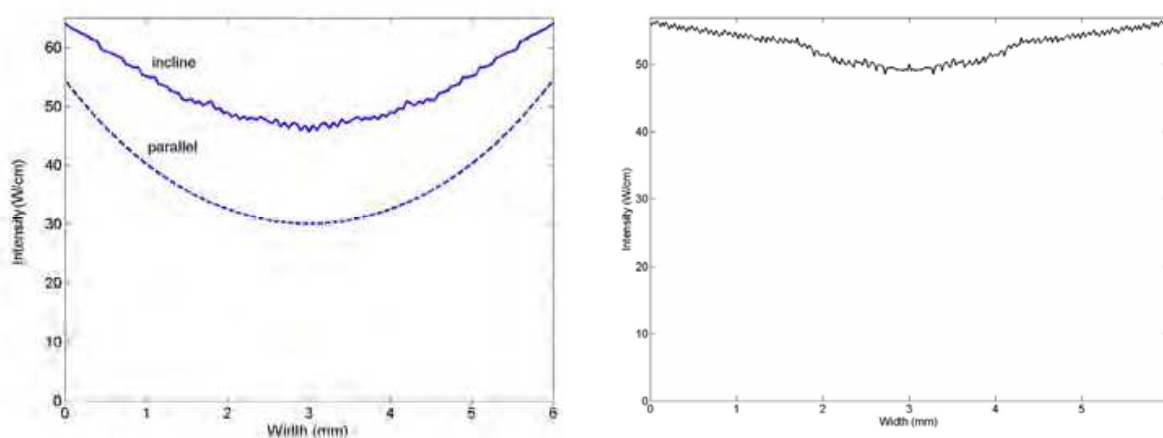

Fig. 1.4. (b). Pump power intensity versus width for plane cladding (left), concave cladding (right).

1.2 Unstable resonator for edge-pumped planar waveguide lasers

One of the most popular unstable resonators is confocal unstable resonators, which have been generally used in the high-power planar waveguide gas lasers [3]. Confocal unstable resonators can provide diffraction-limited output beam in very short cavities with large beam diameters. Detailed investigations on effects of non-uniform pumping with confocal unstable resonators are important in the design of edge pumped solid-state planar waveguide lasers. The characteristics of output laser beam of edge-pumped planar

waveguide solid-state lasers with confocal unstable resonators have been investigated numerically considering pumping non-uniformity, gain saturation and beam interaction. A novel quasi-self-imaging planar waveguide is designed for single-mode output.

While the ray matrix technique gives good descriptions to the beam characteristics in stable resonators, diffraction effects in unstable resonators play an important role and make the analytic solutions unavailable. There are a number of methods, which are mainly extensions of the Fox-Li method for simulation of unstable resonators [4~7]. However, no method can treat all types of unstable resonator due to efficiency, accuracy and divergence of iteration. For an confocal unstable resonator with a large Fresnel number, which is commonly used in planar waveguide solid-state lasers, we explore fast Fourier transform (FFT) techniques [8, 9] with equivalent coordinate transform and saturable gain sheets to investigate the output beam quality of edge pumped planar waveguide solid-state lasers. Optimization of pumping uniformity for good output beam quality and high pumping efficiency is analyzed. The influences of doping concentration, cavity length and effective Fresnel number are also discussed. We find that good beam quality and high efficiency can be obtained with asymmetric pumping and negative branch confocal unstable resonators. The results are useful in design of diode pumped solid-state lasers with unstable resonators.

When the laser beam travels back and forth in the resonator, the laser gain is saturated by the double passed laser beam. As we mentioned above, the forward and backward beams go through the crystal waveguide in different passes. Thus, we apply a linearly expanding coordinate transform [4] in the calculation. For the forward laser beam, the primed coordinate is adopted. The gain medium is divided equally into several slices (gain sheets) with constant small signal gain coefficients. Between two adjacent slices, the wave propagates freely and is described with aid of FFT technique [10]. For the backward laser beam, the coordinate is expanded according to the resonator magnificent factor, but the gain on the axis is considered as constant. Therefore, the gain is saturated from the sum of the forward and backward laser beam, varying the distribution in different slices. The gain saturation is described by [11]

$$u_2(x,z) = u_1(x,z)\sqrt{\exp\frac{g_0\Delta z}{1+[I^+(x,z)+I^-(x,z)]/I_s}} \qquad (1.6)$$

where $u_2(x, z)$ and $u_1(x, z)$ are the complex amplitudes before and after gain slices; I_s is the saturation intensity, Δz is the propagation length in the gain medium, $I^+(x, z)$ and $I^-(x, z)$ are laser intensity for the forward and the backward beam, respectively. The small signal gain coefficient $g_0 = \eta_0 P_{abs}(x)$, where η_0 is a coefficient determined by the quantum efficiency, the stimulated emission cross-section, and the upper level energy transform coefficient. Notice that the x-coordinate for the backward beam should be transformed to the expanding coordinate system.

Without gain saturation, the output beam is well collimated plane waves with nearly constant phase fronts (see Fig. 1.5a). Using edge-pumping, the part of beam near the waveguide edge obtains larger gain than the center part does. The laser beam is pulled to the edge of the waveguide. The output beam diameter is gain-narrowed as shown in Fig.

1.5(b). The beam profile is modulated with an increased phase angle. In a negative branch unstable resonator, the laser beam is reversed when it passes through the intra-cavity focus, i.e., the upper part of the beam swaps with the lower part. In such a way, gain non-uniformity can be averaged by asymmetric pumping when the beam bounces back. As can be seen in Fig. 1.5(c), the main ripple in the output beam profile becomes smoother with asymmetric pumping than that with symmetric pumping. Moreover, the phase aberration is reduced to about 75%. In order to evaluate these effects in only one parameter, we calculated the beam propagation factor M^2 of the output beam.
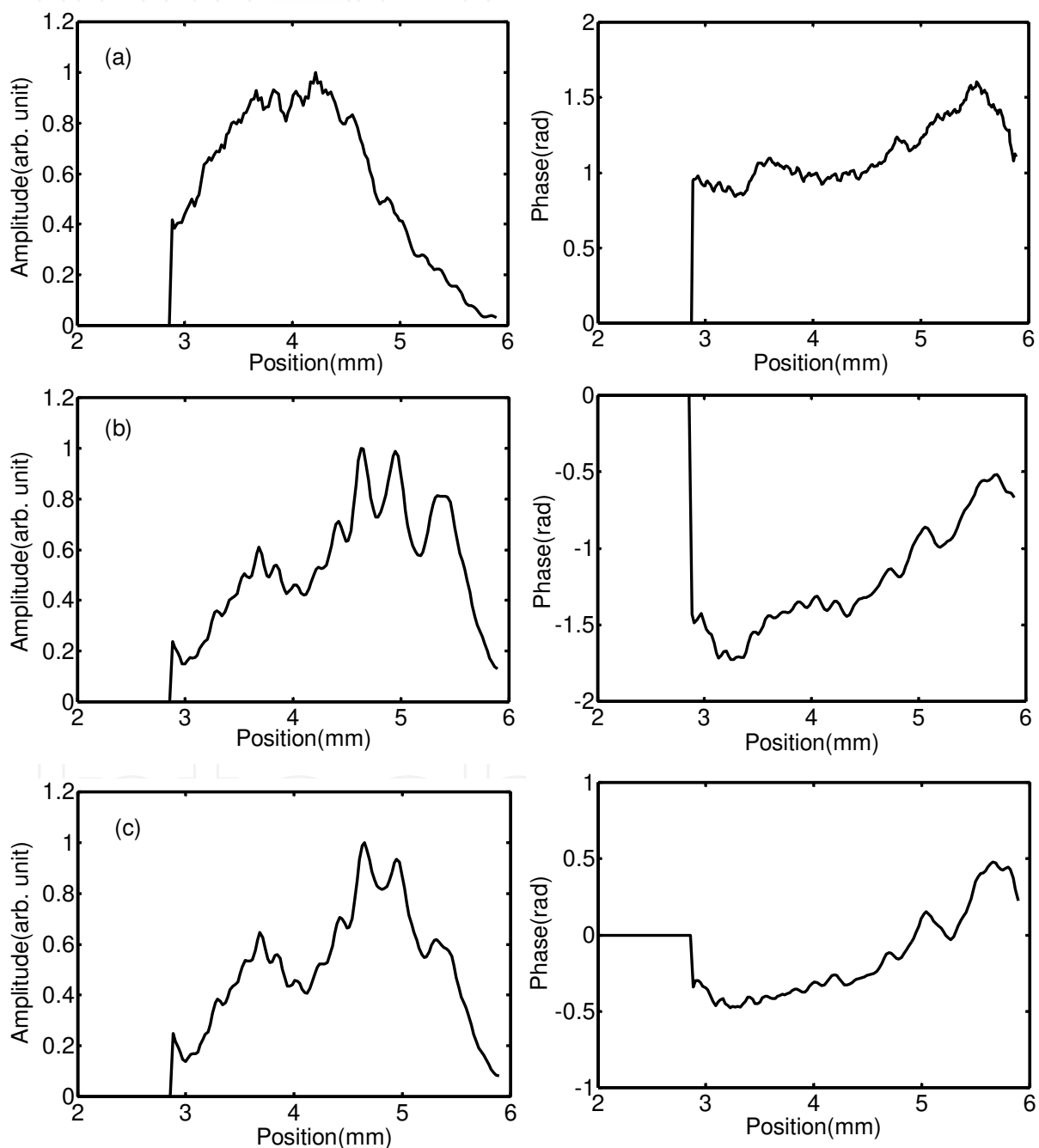

Fig. 1.5. Output beam profiles for (a) bare cavity, (b) symmetric pumping, (c) asymmetric pumping with asymmetric factor b=1.5.

The beam propagation factor M^2 is calculated by propagating the output beam through a long focal length lens. The beam width is defined by the second moment intensity [4].

$$d = 4\sigma_x \qquad (1.7)$$

$$\sigma_x^2 = \frac{\int I(x,z)(x-\overline{x})^2 dx}{\int I(x,z)dx} \qquad (1.8)$$

where $I(x,z)$ is the laser intensity at position z; $\overline{x}$ is the center of the laser beam given as

$$\overline{x} = \frac{\int I(x,z)x dx}{\int I(x,z)dx} \qquad (1.9)$$

The beam waist is calculated by a hyperbolic fit of beam widths at different positions. The beam propagation factors M^2 of the output beam with varying cavity length are shown in Fig. 1.6. With increasing the cavity length, the beam propagation factor displays resonance behavior, which arises from the diffraction nature of hard-edge aperture [10]. The best beam quality can be obtained with an optimum cavity length. This optimum cavity length is the result of combination of pumping non-uniformity, beam control of unstable resonator, and gain saturation.

As we described above, the pumping non-uniformity is enlarged with large absorption coefficients, resulting in bad beam qualities. Using asymmetric pumping could compensate the pumping non-uniformity somewhat by the off-axis resonator, and improve the beam quality then. With an asymmetric factor b=1.5, the beam propagation factor $M^2 \approx 1.25$ is obtained even for the absorption coefficient α=0.5 cm^{-1} (see Fig. 1.6b). Notice that the optimum cavity length is almost independent of the asymmetric factor. In comparison, the beam propagation factor shows $M^2 \approx 1.43$ with an inversed asymmetric factor b=0.6, confirming asymmetric pumping really improving the output beam quality.

The characteristics of output laser beam of edge-pumped planar waveguide solid-state lasers with confocal unstable resonators have been investigated numerically considering pumping non-uniformity, gain saturation, and beam interaction. Optimized methods for cavity length and doping concentration have been given to offer good beam quality and high pumping efficiency. It has been found that good beam quality and high pumping efficient can be achieved by asymmetric pumping and negative branch confocal unstable resonators. These results provide reference for designs of high-power planar waveguide solid-state lasers.

1.3 Single-mode oscillation from quasi-self-imaging multi-mode waveguide

The input beam can reproduces itself at the exit of a self-imaging waveguide [12,13]. Hence, beam quality can be preserved in the laser amplifier made by a self-imaging planar waveguide [14]. Self-imaging planar waveguides associating with self-imaging resonator have also been used in laser oscillators [15]. Because the input and exit beams have the same
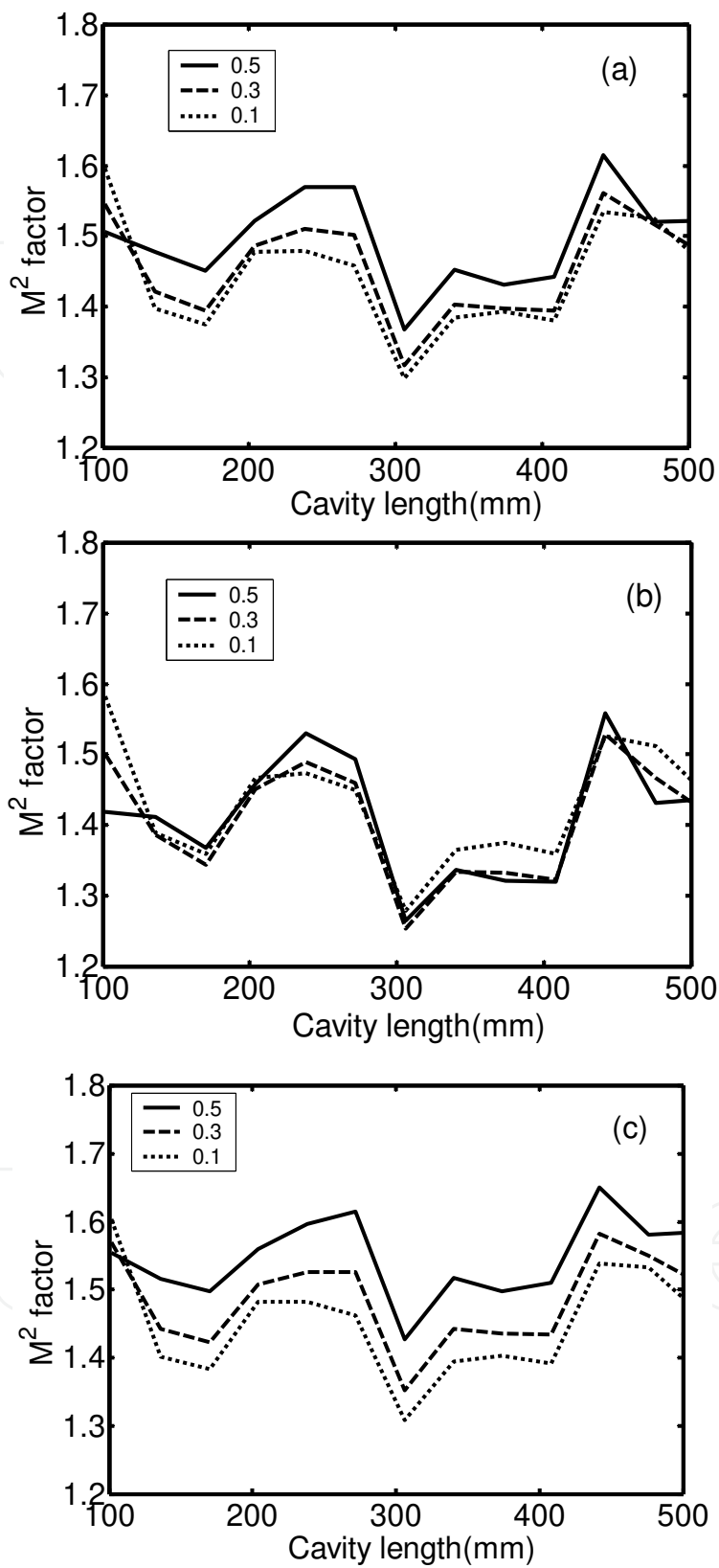
Fig. 1.6. Beam propagation factor M^2 values with symmetric pumping (a) and with asymmetric pumping of $b = 1.5$ (b) and $b = 0.6$ (c).

field profile, single-mode propagation of the laser beam is not necessary in the waveguide. High beam quality is obtained by controlling the beam width at the entrance of the waveguide through optimal resonator design [16].

In this context, we present a novel planar waveguide design, in which self-imaging is incomplete and each guided mode suffers different coupling losses. Single-mode output can be achieved with this quasi-self-imaging planar waveguide. The influence of thermal lens effects on the single guided mode operation is discussed.

The quasi-self-imaging planar waveguide as shown in Fig. 1.7 consists of two parts with different core thicknesses D and d, respectively. Both cores are made by the same rare-earth doped medium surrounded with non-doped cladding. The resonator can be of the plane-plane type fabricated by direct coating on the waveguide facets, or of the hybrid/unstable type with concave mirrors attached to the waveguide ends [2]. The pump light can be coupled from the edges or surfaces into the waveguide. Both the thin and thick waveguide parts support more than one guided mode in the core. The thick waveguide part is constructed with the self-imaging properties while the thin part is a conventional waveguide.
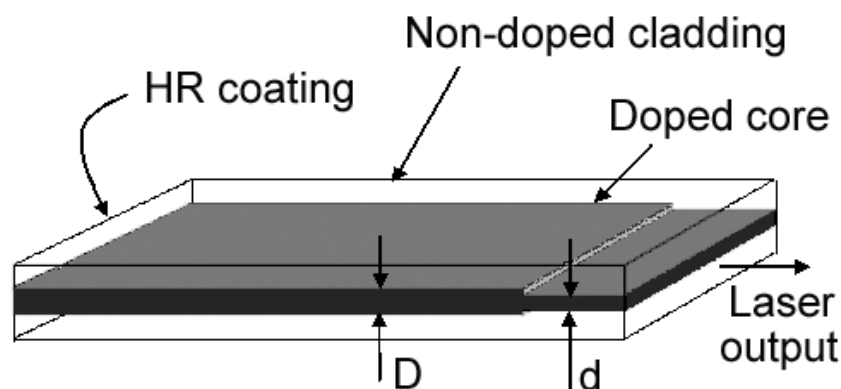

Fig. 1.7. Structure of quasi-self-imaging planar waveguide laser.

For an input field profile Ψ_{in}, the profile Ψ_E at the exit of a multi-mode waveguide of length L is given by the superposition of eigen-modes E_m, [1]

$$\Psi_E = \exp(-jn_{core}k_0L)\sum_{m=0} E_m \exp(j\Delta\beta_m L)\int E_m \Psi_{in} dx \tag{1.10}$$

where n_{core} is the refractive index of the core and k_0 is the wave vector in vacuum. The eigen-mode E_m and the propagation constant β_m can be obtained from the scalar wave equation together with the boundary condition from Maxwell's equations [17]. In the case that the waveguide supports a sufficiently large number of eigen-modes, the field at the exit of the waveguide will reproduce the input field precisely according to Eq. (1.10). However, if a waveguide can support only a few guided modes, the field at the exit can not reproduce the input field precisely. In addition, the propagation constant $\Delta\beta_m$ will be out of proportion to m^2 in a weakly guided waveguide. Thus, the self-imaging in such a waveguide is no longer perfect.

The difference between the exit and input field can be regarded as a kind of coupling loss. Because the quasi-self-imaging waveguide can guide a few modes, the coupling loss is determined by how completely the input field is represented by the guided modes. Thus the coupling loss depends on the input field profile. In an appropriately designed waveguide, the fundamental mode can be the one with lowest loss, so lasers based on such a type of waveguide can provide single fundamental mode output. We note that some fractions of Λ have special self-imaging properties. For instance, as shown in Table 1.2, even modes have the same $\pi/4$ phase shifts, while odd modes show a π phase difference at a propagation distance of $5\Lambda/8$. Actually, the modes have similar phase shift properties at distances equal to an odd multiple of $\pi/8$. In such a way, a symmetric field in a $(2l+1)\pi/8$ long waveguide will still be self-imaged, but an asymmetric field will not.

Mode	TE$_0$	TE$_1$	TE$_2$	TE$_3$	TE$_4$	TE$_5$
Phase shift	$\pi/4$	π	$\pi/4$	2π	$\pi/4$	π

Table 1.2. Phase shifts for several lowest-order modes at a propagation distance of $5\Lambda/8$ [14].

With the symmetry of eigen-mode in mind, the thick waveguide part of the quasi-self-imaging waveguide structure, as described in Fig. 1.7, is designed to be $5\Lambda/16$ long, and a round trip in the thick waveguide part will be $5\Lambda/8$. The eigen-modes of the thin waveguide part are then the input field for the thick waveguide part, i.e., $E_i^{thin} = \Psi_{in}$, where E_i^{thin} is denoted as the ith order mode of the thin waveguide part. When the field travels a round trip in the thick waveguide part, the coupling loss for the ith order mode at the interface between the thick and thin parts is given by [17]

$$\alpha_i = 1 - \int \left| \Psi_E E_i^{thin} \right| dx \qquad (1.11)$$

As described above, odd i modes with asymmetric field profiles have large coupling losses if the thick waveguide part is $5\Lambda/16$ long. To achieve low coupling loss for the fundamental mode we choose the core diameter d close to D, i.e., $d \sim D$, and consequently $E_0^{thin} \sim E_0^{thick}$. When E_0^{thin} enters the thick waveguide part, E_0^{thick} carries most of the power of E_0^{thin}. Because the waveguide length is designed for $2\pi / \Delta\beta_0^{thick}$, the coupling loss of the fundamental mode E_0^{thin} is small, and the laser can be operated with a low threshold. Further, the waveguide with $d \sim D$ has a large active mode volume.

As an example, we calculate the coupling loss for a waveguide composed of a 1.0 at.% Nd-doped YAG (n=1.82) core surrounded with non-doped YAG (n=1.8192) cladding. The core in the thin waveguide part is chosen to be 70 μm thick and 10 mm long, while that in the thick part is 90 μm thick and 38.8 mm long. The total thickness is 1 mm. In this waveguide, the thin and thick parts can guide 7 and 10 TE modes, respectively. In Fig. 1.8, field profiles at propagation distances $5\Lambda/16$ and $5\Lambda/8$ are compared with the initial field profiles for the three lowest eigen-modes E_0^{thin} of the thin waveguide part. Clearly, self-imaging of the fundamental mode at a distance of $5\Lambda/8$ is better than that of higher-order modes. The coupling losses are calculated according to Eq. (1.11) for a

set of eigen-modes E_i^{thin} and shown in Fig. 1.8(a). The coupling loss for the fundamental mode is about 0.026. In comparison, the losses for higher-order modes are all larger than 0.3.

Due to smaller beam width, the coupling loss of the fundamental mode increases more slowly than that of higher order modes. Thus, mode discrimination can be improved by using a little longer waveguide. For example, the coupling loss for a waveguide with a 42-mm-long thick part is shown in Fig. 1.8(a) (filled dots). The coupling loss of the fundamental mode is about 0.04 while that of the second order mode is 0.7.
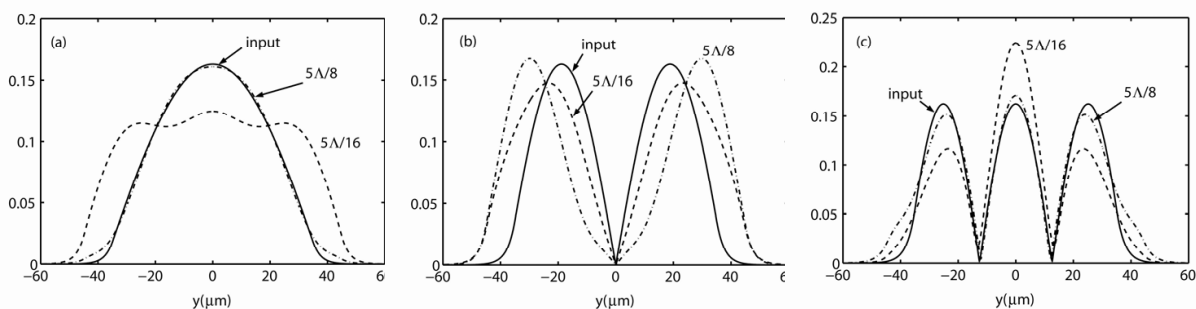
Fig. 1.8. Field profiles of eigen-modes compared with the field profiles at a distance $5\varLambda/16$ and $5\varLambda/8$ for (a) mode i=0, (b) i=1, (c) i=2.

In the multi-mode waveguide lasers, all modes compete through the gain saturation. The photon density of ith order mode is given by the multi-mode rate equations [17]

$$\frac{dI_i^{thin}}{dz} = \left[\frac{g_0}{1 + I/I_s} - \alpha_i^{thin} \right] + I_{spon}$$ (1.12a)

$$I = \sum_i \left[I_{i+}^{thin} + I_{i-}^{thin} \right]$$ (1.12b)

where I_+ and I_- are the photon intensity of laser beam propagating in forward and backward direction, respectively; α_i^{thin} is the coupling losses of ith order mode, g_0 is the small signal gain, I_s is the saturation intensity, and I_{spon} is the contribution of spontaneous emission. Substitute the coupling losses into Eq. (1.12), we obtain evolution of photon density of each mode with varying the pump power. In the calculation, a uniform gain is assumed in both thin and thick waveguide parts. The gain saturation is included by insert 10 gain sheets in the middle of the propagation. As can be seen in Fig. 1.9, more than 95% of laser power has been caught by the fundamental mode after a few round trips. Even for the Q-switched planar waveguide lasers, it is sufficient to achieve single mode operation.

2. High-power Nd:YAG planar waveguide lasers

Rapid progress has been made in fiber lasers, thin-disc lasers and slab lasers in recent years. A variety of medium have been used to fabricate planar waveguide. Crystal or ceramic
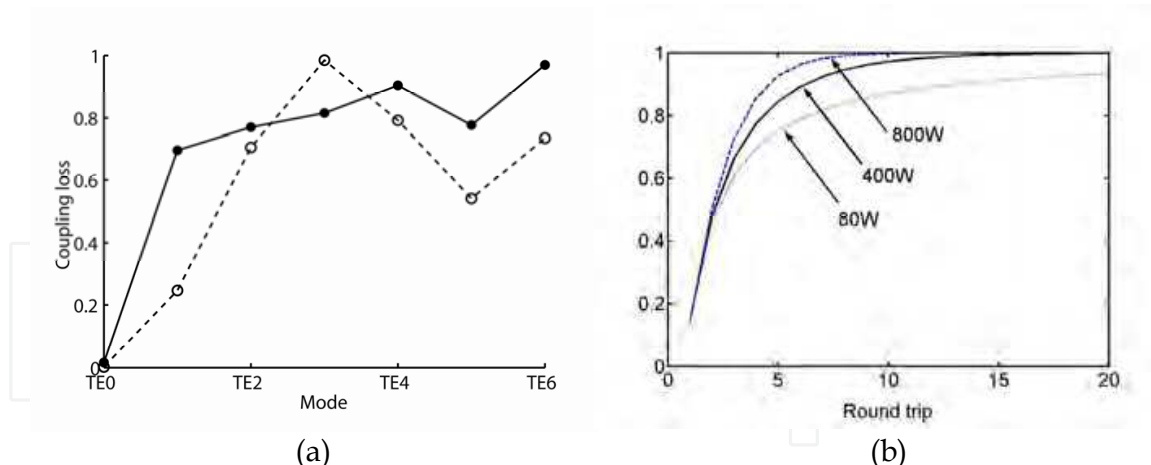
Fig. 1.9. (a) Coupling losses of eigen-modes for 38.8 mm (=5Λ/16) long (empty dots) and 42 mm long (filled dots) thick waveguide part. (b) Laser power percent carried by the fundamental mode as a function of time for various pump power.

Nd:YAG is one of the most popular active material used for high-power planar waveguide lasers. Compared with fiber and thin-disc lasers, planar waveguide lasers are advantageous such as compact, two-dimensional power scalable and easily integrated. The potential of planar waveguide lasers has been exploited broadly. Double clad concept, sandwich structure and quasi self-imaging structure have been applied to high power planar waveguide lasers [13, 18, 19]. The output beam quality of high power solid-state laser usually suffers from the thermal disturbance in the laser host. The temperature gradient along the width of slab gives rise to optical distortions. How to remove the waste heat and reduce the thermal effects efficiently usually are main considerations in the design of high average power systems. In related articles [20], consequences of thermal and thermo-mechanical effects have been discussed for slab lasers and amplifiers. The analyses of nonlinear thermal effects in slab lasers are also presented in ref. [21]. In this context, we describe some experimental investigations on the high average power Nd:YAG lasers.

2.1 High-power Nd:YAG planar waveguide lasers with YAG and Al$_2$O$_3$ coatings

Thermal distortion and pumping non-uniformity in the high-average-power solid-state lasers are serious limitations for achieving good beam quality in using unstable resonators. Using thin slab geometry with large aspect ratio, heat removal can be very efficient. The thermal lenses, thermal birefringence, and their aberration are compensated by zig-zag path of the laser beam. As a type of thin slab lasers, the planar waveguide laser guides the laser beam by refractive index step. The beam distortion induced by thermal effects is resisted by guidance condition. Single-mode waveguides and suitable waveguide resonators can hold near-diffraction limited beam quality in the transverse waveguide axis, whilst unstable resonators are required to match the high Fresnel number in the lateral (width) axis. Pump and cooling non-uniformities exacerbate the optical distortions in the solid-state lasers. Compensation for these non-uniformities is important to obtain high efficiency and good beam quality output.

The planar waveguide laser uses a very thin rare-earth doped core as the active layer, where the heat dissipated in the waveguide can be removed efficiently from its large area surfaces.

The planar waveguide lasers are generally fabricated in symmetrical structures [10, 22~24], where an active core is in the middle of the waveguide and the claddings are symmetrically bonded to the core from two sides. Non-symmetrical structures have also been applied for the planar waveguide lasers [25, 26]. In this section, a planar waveguide laser with simple non-symmetrical structure is proposed to reduce the thermal effects. With non-symmetrical design, heat removal can be improved by directly contacting the active core to the heat sink. In order to improve pump uniformity and absorption efficiency, the pump light is injected at a small oblique angle to the edge of planar waveguide, and then the light follows a zigzag path along the slab. The thermal effects of different cladding materials are discussed. With appropriate cladding materials, the thermal and thermal-mechanic influences can be alleviated.

The structure of non-symmetrical planar waveguide is shown in Fig. 2.1. The ion-doped active core is directly contacted to the heat sink. To preserve the total internal reflection at the bottom surface, a very thin coating is applied between the active core and the heat sink. The pump light is injected to the planar waveguide at a small oblique angle. Since the pump light projects on different position through the un-doped cladding, the exponential absorption of pump power along the width direction is flatted, resulting in uniform pumping and high absorption efficiency. The oblique angle can be estimated from $a = \arctan(T/W)$, where T and W are the thickness and width of waveguide, respectively. In the experiments, the oblique incident angle is calculated around 5 degree. When the pump light is focused into the waveguide, the convergence angle also influences the path of ray inside the waveguide. In Fig. 2.2, the pump intensity along the width direction is plotted for various convergence angle of the focused pump light. When the convergence angle is less than 20 degree, the pump distribution is quite uniform. Compared with the exponential absorption where the maximum pump intensity is at the edge of waveguide [10], the maximum pump intensity moves to the middle of waveguide by the oblique edge-pumping. As it is well known, the edge of slab bears the largest thermal stress. Thus, the thermal stress at the edge is released to some extent with the oblique edge-pumping.
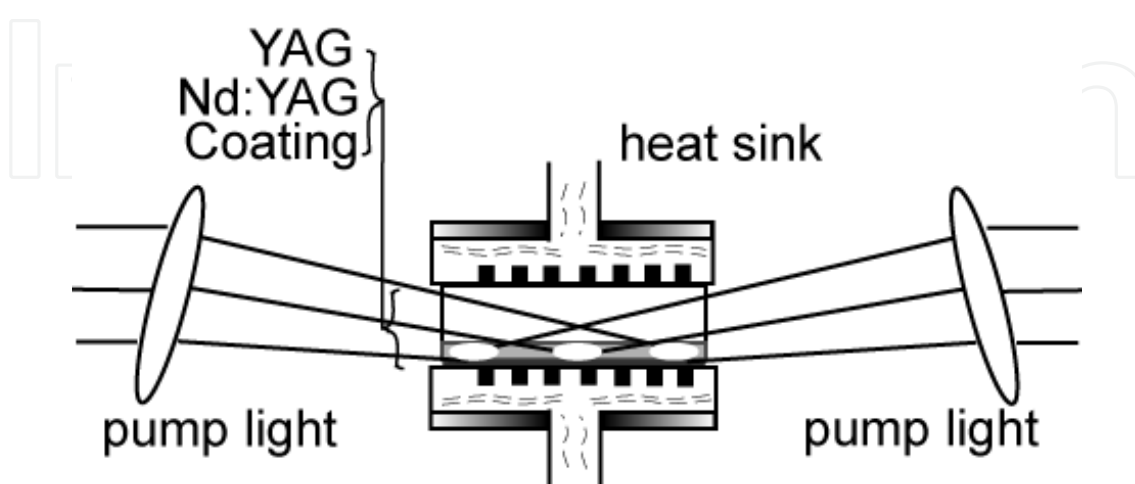

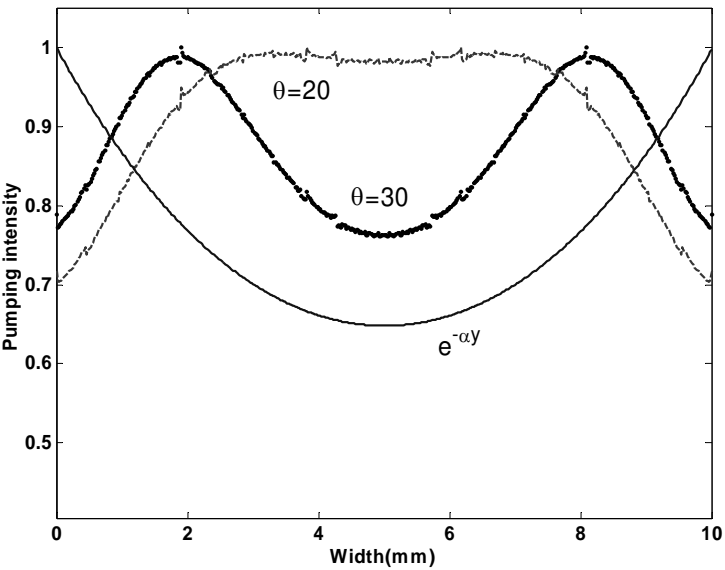Fig. 2.1. Oblique edge pumping of planar waveguide.

Fig. 2.2. Pump intensity along the width direction when the focused pump light is launched into the waveguide with the oblique angle of 5 degree. The convergence angles of the focused pump light are 20 and 30 degree, respectively. The solid line is for exponential absorption of the pump light.

With oblique edge-pumped technique, the thermal effect along the thickness is considered. We assume the y-axis direction along the thickness and the origin is taken as the center of the core. The thickness of waveguide core is $2h$, and the thickness of upper and bottom claddings are d_1 and d_2, respectively. The corresponding thermal conductivity and the surface heat transfer coefficient are k_1, λ_1 and k_2, λ_2, respectively. The planar waveguide is clipped by the copper micro-channel heat sink from the upper and bottom surfaces. The temperatures on the surfaces of upper and bottom claddings are supposed equal to that of the coolant. Heat flow in the waveguide is then a one-dimensional function. The thermal equation is [17]

$$\nabla^2 T = \frac{\partial^2 T}{\partial y^2} = -\frac{Q}{k} \tag{2.1}$$

where k is the thermal conductivity of the core, and Q is the heat generated per unit volume. The boundary conditions between the core and the cladding are [27]

$$\left. \frac{dT}{dy} \right|_{y=\pm h} = \pm \frac{\lambda_{(1,2)}}{k}(T_l - T_s) \tag{2.2}$$

where T_s is the temperature at the core boundary, and T_l is the temperature at the cladding. We define the effective thickness $L=(\lambda_1 k_2/\lambda_2 k_1)d_2+d_1+2h$ and the difference in the cladding thickness $S=d_1-(\lambda_1 k_2/\lambda_2 k_1)d_2$. The analytical solutions is given by

$$T_b(y) = \frac{\lambda_1 Q h}{\lambda_2 k_1}(1 + S/L)(y + h + d_2) + T_c \tag{2.3a}$$

$$T_c(y) = -\frac{Q}{2k_2}y^2 + \frac{QhS}{k_2 L}(y + h + \frac{\lambda_1 k_2}{\lambda_2 k_1}d_2) + \frac{Qh}{k_2}(2h + \frac{\lambda_1 k_2}{\lambda_2 k_1}d_2) + T_c \qquad (2.3b)$$

$$T_u(y) = Qh(\frac{S}{k_2 L} - \frac{1}{k_2})(y - h - d_1) + T_c \qquad (2.3c)$$

where $T_b(y)$, $T_c(y)$ and $T_u(y)$ are the temperature distributions in the bottom cladding, the active core and the upper cladding, respectively. The temperatures along the thickness direction in the non-symmetrical and symmetrical waveguide lasers are shown in Fig. 2.3. The temperature distribution in the active core is quadratic and linear in the claddings. The highest temperature is given as

$$(T_{max} - T_c)\frac{k_2}{2Qh} = h(\frac{d_1 + h}{L})^2 + \frac{d_1 + h}{L}\frac{\lambda_1}{\lambda_2}\frac{k_2}{k_1}d_2 \qquad (2.4)$$
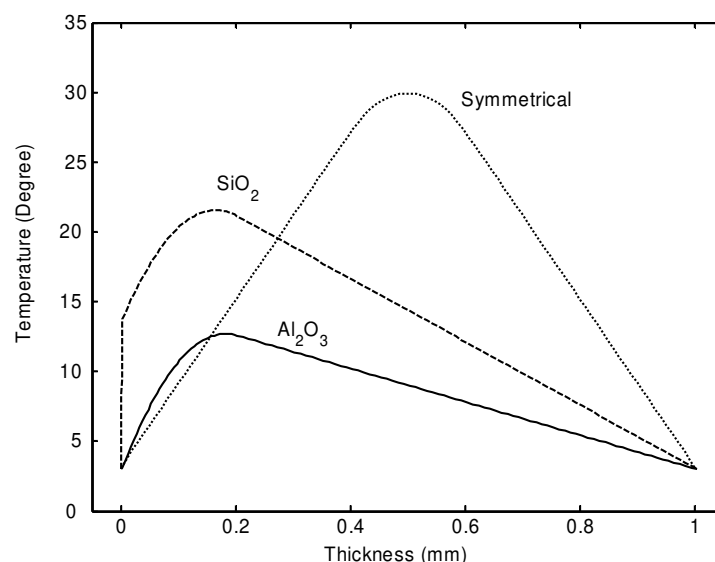

Fig. 2.3. Temperature distributions in non-symmetrical waveguides with Al_2O_3 and SiO_2 coatings, respectively, in comparison with that of symmetrical waveguide when pump power is 1 kW.

in which T_c is the temperature of coolant. The maximum temperature is located at $y = hS/L$. The active core made by 1.0 at.% Nd-doped YAG is 0.2 mm in thickness, while the upper cladding is a 0.8 mm un-doped YAG layer. The bottom cladding is a coating of about 3-μm thick. The condition about SiO_2 bottom coating has been discussed in the work [26]. The material SiO_2 has great differences in the thermal conductivity and the surface heat transfer coefficient with YAG. The material SiO_2 is not a good material for the planar waveguide laser with non-symmetrical structure. Changing bottom cladding material as YAG or Al_2O_3, it is found that the maximum temperature decreases rapidly and the location of the maximum temperature keeps almost the same. Considering maturity in the vacuum coating technology, Al_2O_3 is a prefer choice. The temperature with Al_2O_3 coating is only a half of that with SiO_2 coating (see Fig. 2.4).
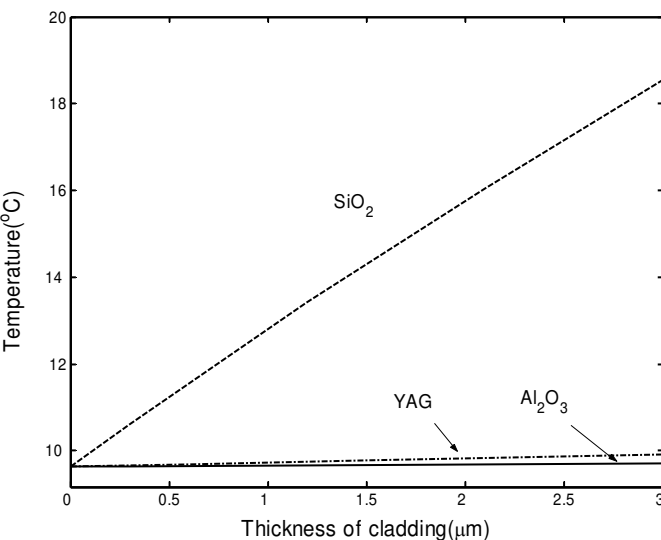
Fig. 2.4. The highest temperature in the waveguide verses coating thickness for Al_2O_3, YAG and SiO_2 coatings when pump power is 1 kW.

Due to the rectilinear pumping and the cooling of the waveguide, the thermal gradient and thermally induced stress are present only in the y-axis direction. The thermal stress caused by the thermal gradient ΔT is given by [17]

$$\sigma = \frac{\beta E}{(1-\nu)} \Delta T \tag{2.5}$$

where β is thermal expansion coefficient; E is Young's modulus; and ν is Poisson's ratio. The values of the material parameters for Al_2O_3, YAG, or SiO_2 are listed in Table 2.1. The thermal stress distributions for non-symmetrical waveguide with Al_2O_3, YAG, or SiO_2 coatings are shown in Fig. 2.5. The stress in the center of waveguide is positive (compressive stress) while it is negative (tensile stress) near the surfaces. In the Nd:YAG planar waveguide with SiO_2 coating, there is much stronger stress of 630 kg/cm² at the edge due to higher temperature in the waveguide. While in the waveguide with Al_2O_3 or YAG coating the value is 300 kg/cm², only a half of that in the waveguide with SiO_2 coating. This is only one-sixth of fracture strength for YAG crystal of 1800~2100 kg/cm². Furthermore, although the non-symmetrical structure results in the non-symmetrical temperature distribution, the waveguide with Al_2O_3 and YAG coating have nearly the same tension at the edges with the value about 300 kg/cm², whereas the waveguide with SiO_2 coating shows a large non-balanced stress. The thermal deformation with the SiO_2 coating is more severe than that with the Al_2O_3 and YAG coatings.

	thermal expansion coefficient α (10-6/K)	Young's modulus E (106 kg/cm2)	Poisson's ratio ν
Al_2O_3	5.6	4.26	0.309
YAG	6.1	3.17	0.25
SiO_2	0.55	0.73	0.17

Table 2.1. thermal properties of Al_2O_3, YAG, and SiO_2 coatings [17]

As shown in Table 2.1, the thermal expansion coefficients of Al_2O_3 and YAG material are one order of magnitude larger than that of SiO_2. Thus, the tension inside the SiO_2 coating is much smaller than that inside Al_2O_3 and YAG coatings (see Fig. 2.5b). However, difference in the thermal expansion coefficient between SiO_2 and YAG results in large shear stress at the core boundary. Obviously, the Al_2O_3 and YAG coatings are better matched to the Nd:YAG core.
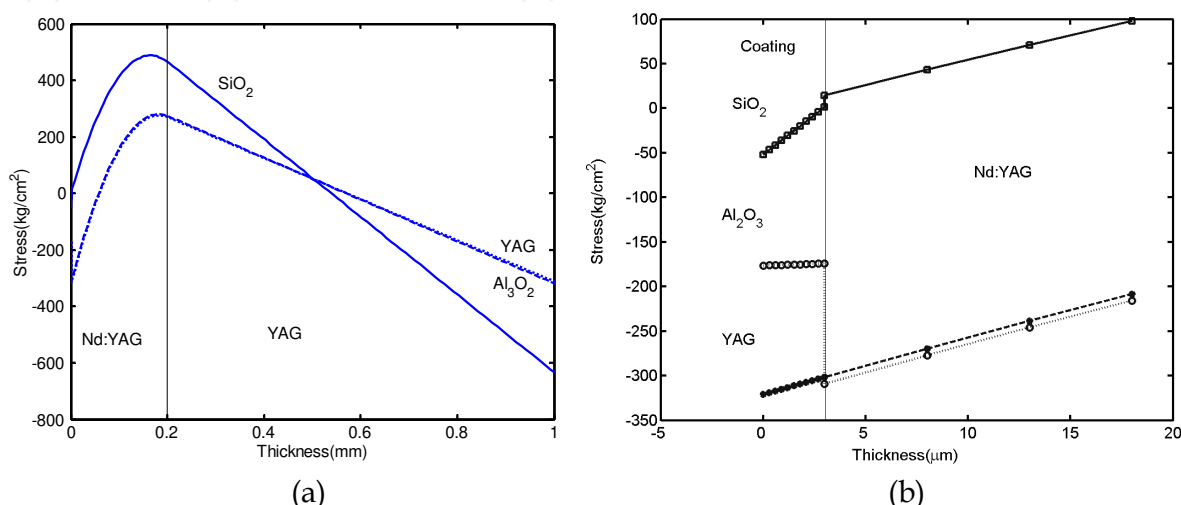

Fig. 2.5. (a) Stress distributions inside non-symmetrical waveguides with Al_2O_3, YAG and SiO_2 coatings. The curves for YAG and Al_2O_3 coatings are almost overlapped. (b) Stress near the bottom surface for waveguides with the Al_2O_3, YAG and SiO_2 coatings when pump power is 1 kW. Vertical lines refer to the interface of Nd: YAG and YAG.

The non-symmetrical Nd:YAG planar waveguide laser was installed as shown in Fig. 2.6. The planar waveguide is 58×10×1 mm in dimension with 3-μm thick Al_2O_3 coating on the bottom. Two laser diodes (LD) with emission area about 10×48 mm can deliver 640 W average power with 200-μs duration and 1 kHz repetition rate after fast-axis collimation. Two cylindrical lens (f_1=50 mm and f_2=20 mm) were used to launch the pump light into the waveguide. The divergence angle of the pump light is less than 20 degree and the incident angle to the x-axis is around 5 degree. About 90% pump power can be coupled into the waveguide. A 100-μm thick indium foil is sealed between the heat sink and waveguide to ensure a uniform thermal contact with the heat sink. Water flux in the micro-channel heat sink is about 4 l/min and the temperature of coolant is set to 18 °C.

A plane-parallel cavity was used in the first place. Two flat mirrors were placed 1-mm apart from waveguide facets. The experimental output power versus the pump power for various output couplers is shown in Fig. 2.7(a). A maximum average power of 310 W was obtained with the output coupling of 28%. A hard-edge positive unstable resonator was constructed to improve the beam quality [13, 19]. The resonator magnification was designed to be 1.4. A concave mirror with 360-nm radius-of-curve of 360 mm and a cut-away convex mirror with 240-nm radius-of-curve were used as the rear mirror and the output coupler, respectively. The output power decreases to 280 W with a slope efficiency of 38%, but the beam quality factor was improved to M^2 =1.5 in the width direction. Roll-over due to the thermal effects was not observed in the experiments. As presented in Fig. 2.7(b), the output power decreases linearly with the stepping down the repetition rate in the same LD current. This

means the loss caused by the thermal distortion is not significant at high repetition rate operation.
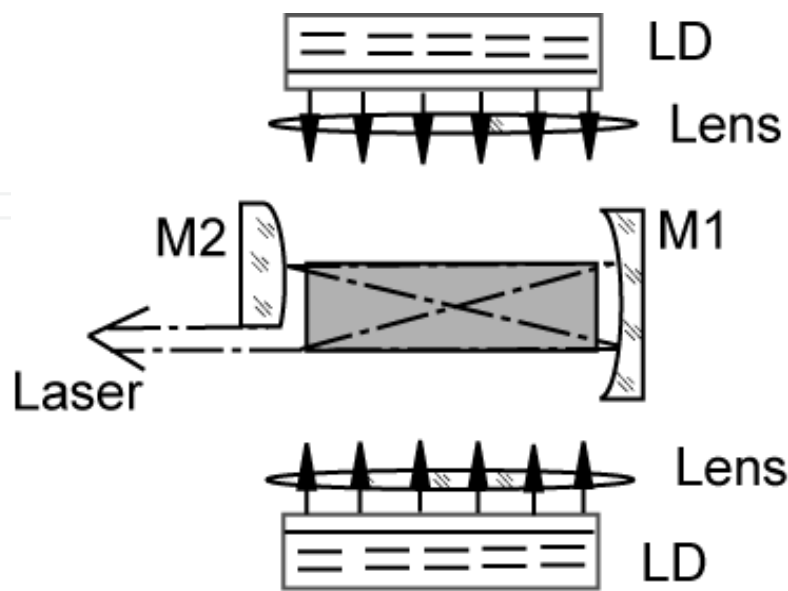

Fig. 2.6. Installation of non-symmetrical Nd:YAG planar waveguide laser.
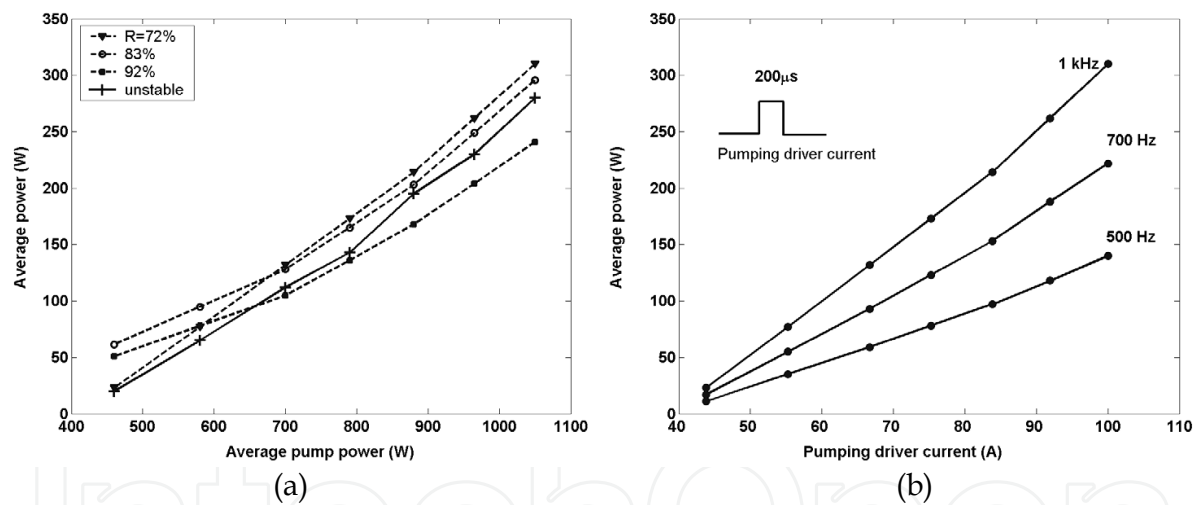

(a) (b)

Fig. 2.7. (a) Experimental output power versus the pump power for plane-parallel and unstable cavities. (b) Change of output power with the repetition rate of pumping.

Using non-symmetrical claddings in planar waveguide lasers can reduce the thermal distortion in high-power regime. Uniform and efficient pumping can be obtained by oblique injection to the edge of planar waveguide. Calculations based on the thermal equations show that, even for the very thin coating, the thermal conductivity and thermal transfer coefficient are important to the heat removal. Applied Al_2O_3 coating to the non-symmetrical planar waveguide, the maximum temperature reduces to only a half of that in the planar waveguide with SiO_2 coating. In the last, we have experimentally demonstrated a high-power Nd:YAG planar waveguide laser with YAG and Al_2O_3 claddings. An average power of 280 W with a slope efficiency of 38% has been obtained in a positive unstable resonator. The output beam quality factor is about $M^2 = 1.5$.

2.2 Passively Q-switched planar waveguide lasers

In some industrial applications, *e.g.*, drilling, cutting, and material processing, pulsed lasers with high peak power and high repetition rate are desired. The technique to achieve huge pulsed laser output is known as Q-switching. Depending on whether the quality Q is altered by external drivers, the laser can be referred as active or passive Q-switching. In comparison with active Q-switching, passively Q-switched lasers offer advantages of low-cost, reliability, and simplicity of operation and maintenance [29, 30]. Passive Q-switching is extensively applied in compact DPSSL. In this section, we describe a high-power passively Q-switched Nd:YAG thin slab laser. A Cr^{4+}:YAG microchip is adopted as saturable absorber mirror in this thin slab laser. The design of thin slab lasers with diffraction limited beam quality is discussed. Average output power of 70 W with a slope efficiency of 36% is obtained.

The experimental setup was depicted in Fig. 2.8, where the Nd:YAG crystal slab is $1\times10\times60$ mm in size and Nd^{3+} ion doping concentration is 1.0 at.%. The slab was clamped by micro-channel heat sinks from two large surfaces (i.e., 10×60 mm surfaces). A 100-μm thick indium foil was filled between the crystal slab and the heat sink in order to reduce the thermal and mounting stress. The temperature of cooling water was set to 20°C. The cooling water flowed parallel to the laser propagation direction in the micro-channel heat sink, reducing the temperature gradient through the cross section of slab. To minimize the mounting stress during assembly, mount of the slab on the heat sink was monitored by an interferometer. Aberrant fringes should be eliminated by adjusting the locking screws. The dimension of a finished laser head was about $60\times74\times150$ mm.
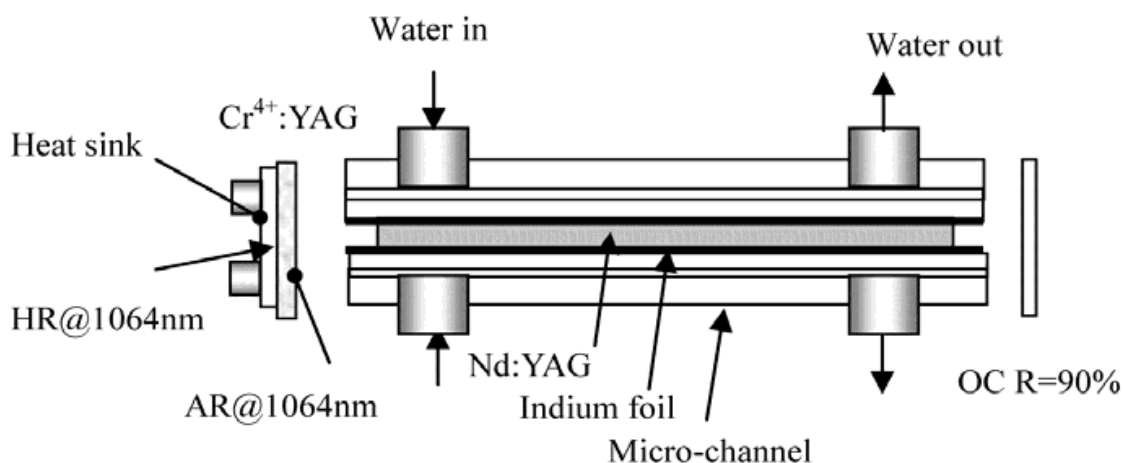

Fig. 2.8. Experimental setup of passively Q-switched thin Nd:YAG slab lasers.

The laser is passively Q-switched by a Cr^{4+}:YAG micro-chip with size of $0.5\times5\times15$ mm. One surface of the Cr^{4+}:YAG chip is HR (high reflectivity) coated while another one is AR (anti reflectivity) coated at 1.06 μm. Thus, the Cr^{4+}:YAG micro-chip acts as a saturable absorber mirror in the slab laser. The initial transmission of the Cr^{4+}:YAG saturable absorber mirror is 90%. Since the slab laser is designed working in high power regime, the Cr^{4+}:YAG chip is compulsively cooled by a micro-channel heat sink attached to its back surface.

In order to acquire single mode oscillation in compact resonator, we control the pump beam diameter to match the fundamental laser mode inside the Nd:YAG slab. In such a way, higher order modes will be filtered out due to lower gain outside the pump range. For the plane-parallel resonator adopted in our experiment, the fundamental mode beam radius calculated from *ABCD* matrix method is shown in Fig. 2.9 as a function of the thermal refractive power. The laser works in the range shaded in Fig. 2.9. The laser beam radius inside the slab is about 0.2 mm, so we designed the pump beam radius to be 0.25 mm and chose the Nd:YAG slab of 1 mm in thickness.

Two horizontal laser diode (LD) arrays, of which each consists of three LD bars, closely pump the slab from both edges. Micro cylindrical lenses of 600 μm in diameter are employed to collimate the pump beam from the LD arrays. The emitted pump beam was about 0.5 mm ($1/e^2$) in diameter with the divergence angle of 2°. The pump beam from two edges was adjusted carefully to be in a same plane.

An important feature of thin slab lasers is that the thermal fracture limit is greatly improved. The distributions of temperature and stress in the slab were analyzed numerically to ensure the laser operating safely. The heat removal of the micro-channel heat sink was compared with that of the non-micro-channel heat sink. The micro-channel heat sink was manufactured with channel's diameter of 0.5 mm, length of 55 mm and pitch of 1.5 mm, respectively. The non-micro-channel heat sink was made by drilling a single hole of 5-mm in diameter in a copper block. In Fig. 2.10, we compared the focal length of the thermal lens when different heat sinks were used. Since heat removal with the micro-channel heat sink was more efficiently, the thermal focal length was longer. Furthermore, when using the non-micro-channel heat sink in the slab laser, the laser output power rolled back after the pump power reached 110 W, revealing serious thermal distortion in the crystal slab.
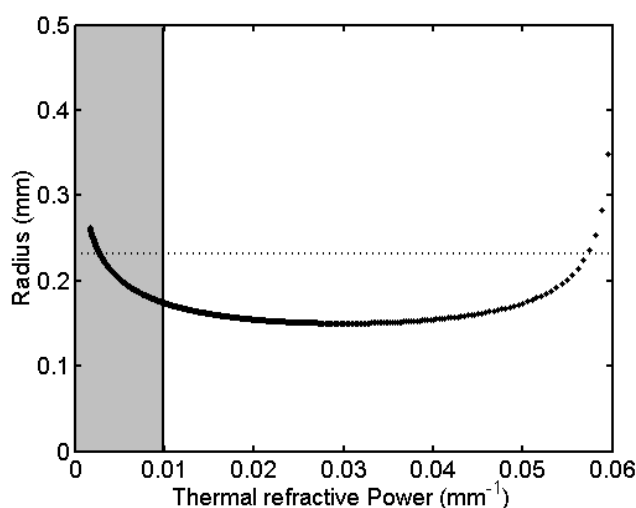

Fig. 2.9. The beam radius of fundamental mode in the center of slab varies with the thermal refractive power. The dotted line indicates the radius of the pump beam. The laser works in the shaded region.
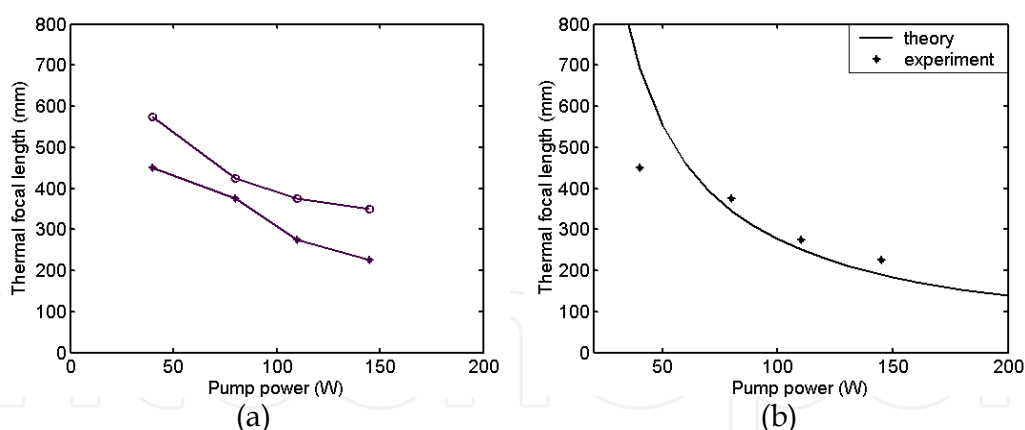
Fig. 2.10. (a) Thermal focal length with different heat sinks. *: non-micro-channel heat sink; o: micro-channel heat sink; (b) Measured and calculated thermal focal length.

After the temperature distribution in the slab being obtained, we can calculate the thermal focal length by assuming a grade-index lens of the pumped slab. The calculated and measured thermal focal lengths in the thickness direction using the micro-channel heat sink are shown in Fig. 2.10. The thermal focal length in the thickness direction was about 140 mm with 200-W pump power. Substituting the thermal focal length into *ABCD* matrix and as shown in Fig. 2.9, we found the requirement for single-mode oscillation was satisfied.

To achieve higher repetition rate and higher output power, it is needed high initial transition of the saturable absorber. The rate equations describing the passively Q-switched laser operation are [27]

$$\frac{d\phi}{dt} = \frac{\phi}{t_r}\left[2\sigma Nl - 2\sigma_s l_s - 2\sigma_e(N_{s0} - N_g) - \ln\frac{1}{R} - \alpha_L \right] \qquad (2.6a)$$

$$\frac{dN}{dt} = W_p - \gamma\sigma cN\phi - \frac{N}{\tau} \qquad (2.6b)$$

$$\frac{dN_g}{dt} = -\frac{A}{A_g}\sigma_g cN\phi + \frac{N_{s0} - N_g}{\tau_s} \qquad (2.6c)$$

The parameters used for above equations are listed in Table 2.2. The condition to produce giant pulse is [31]

$$\frac{d^2\varphi}{dn^2} > 0 \qquad (2.7)$$

Combining Eq. (2.6) with (2.7), we get the maximum initial transition of the saturable absorber as

$$T_{0\max} = \exp[-\frac{L + \ln\frac{1}{R}}{2(\frac{A}{A_s}\frac{\sigma_g}{\gamma\sigma}(1 - \frac{\sigma_e}{\sigma_g}) - 1)}] \qquad (2.8)$$

The maximum transition was calculated as $T_{0\max} = 96\%$. Considering the cost of fabrication, we chose 90% of initial transition of the saturable absorber. The doping concentration of Cr^{4+}

ions was then calculated from N_{s0}=-ln$T/\sigma_g l_s$. Fig. 2.11(a) shows the evolution of the intracavity photon density and the population inversion density in the gain medium. The giant pulse occurs when the saturable absorber is saturated to transparent and the photon density reaches the maximum. From the calculation, we founded the repetition rate higher than 10 kHz. The measured pulse sequences at 220-W pump power are shown in Fig. 2.11(b). The pulse duration is about 10 ns, resulting in the peak power of 0.7 MW. The peak power fluctuation from pulse to pulse is about 5%. The agreement between the calculation and experiment is very well.

Symbol	Parameter	Value
ϕ	intracavity photon density	
N	population inversion density of gain medium	
N_g	ground-state population density of saturable absorber	
N_{s0}	Total population density of saturable absorber	7.0×10^{17} cm^{-3}
γ	inversion reduction factor	1 for Nd:YAG
A	Beam cross-section area in gain medium	
A_s	Beam cross-section area in saturable absorber	
σ	stimulated emission cross section	2.8×10^{-19} cm^2
σ_g	ground state cross section of saturable absorber	4.3×10^{-18} cm^2
σ_e	excite state cross section of saturable absorber	8.2×10^{-19} cm^2
L	length of laser crystal	60 mm
l_s	thickness of saturable absorber	0.5 mm
τ	lifetime of upper laser level of gain medium	230 μs
τ_s	lifetime of excite state of saturable absorber	3.4 μs
t_r	cavity round-trip time	$2nL/c$
R	reflectivity of output coupler	
α_L	intracavity round-trip dissipative optical loss	0.04
W_p	volume pump rate into upper laser level	4.4×10^{21} s^{-1}cm^{-3}

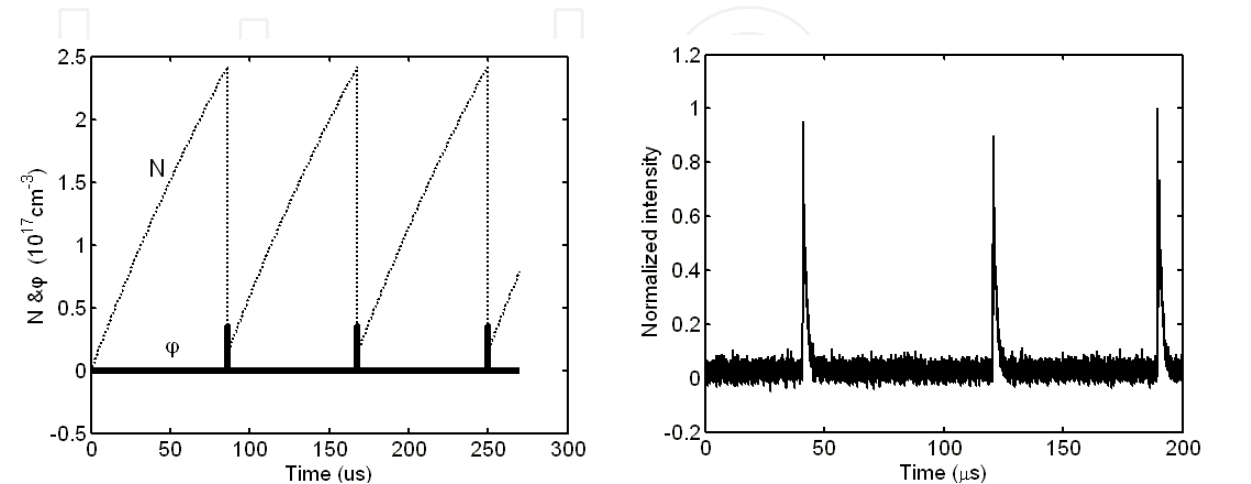Table 2.2. Parameters used in Q-switching equations.

Fig. 2.11. (a) Temporal evolution of intracavity photon density and population inversion, (b) Measured passively Q-switched laser pulse sequence.

Various output couplers were used in the experiments. Output power versus pump power with output coupling of 5%, 9%, 17% are compared in Fig. 2.12. The threshold of pump power is around 10 W. With the optimized output coupling of 9%, the maximum average power of 70 W has been achieved with a slope efficiency of 36% when the pump power is 220 W. Output laser power grows linearly with increasing the pump power. The thin slab laser would be scalable to more than 300 W with 1-kW pump power be used. The beam propagation factor M_y^2 in the thickness direction is 1.4, indicating near single-mode oscillation in the thickness direction. In the width direction, the beam profile is multi-mode due to the weakness of the plane-parallel resonator. If unstable resonator or graded reflectivity mirrors are adopted, good output beam quality in the width direction can be acquired.
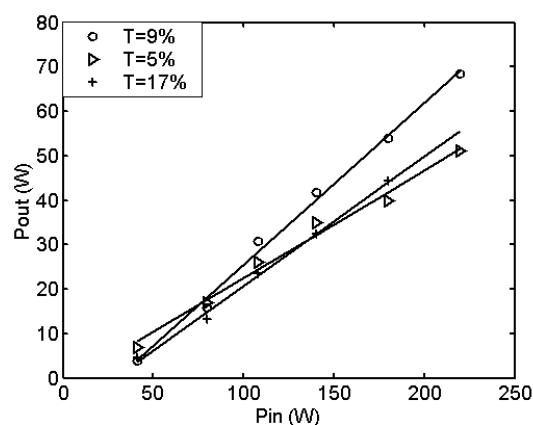

Fig. 2.12. Output laser power versus pumping power.

Thin Nd:YAG slab laser passively Q-switched by Cr^{4+}:YAG microchip is a cost effective approach to high-peak-power, high-repetition-rate solid-state lasers. Output average power of near hundred watts with a slope efficiency of 36% has been acquired with the repetition rate higher than 10 kHz and the pulse width around 10 ns. Near diffraction limited beam quality in the thickness direction has been obtained by precise control of the pump beam width inside the slab. An obvious advantage of this kind of lasers is their relatively compact design with the footprint less than 100 mm^3 and simple replacement of every part. It will find wide applications in industrial and medical fields.

2.3 Acousto-optical Q-switched planar waveguide lasers

In a planar waveguide laser, the laser beam is represented by a set of guided modes in the waveguide, while it propagates in the free space outside. Transform between guided modes and free-space propagation at the waveguide entrance leads to coupling losses and energy exchange among the guided modes. These effects cause competition of the guided modes in the Q-switched planar waveguide lasers. The mode competition enlarges the pulse-to-pulse instability, and distorts the transverse beam patterns.

The crystal waveguide used in the experiments is 11 mm wide and 60 mm long with a 0.2-mm thick Nd:YAG core sandwiched by 0.4-mm thick undoped YAG claddings. The crystal waveguide can support 26 TM modes. Pump light from 10 LD bars with 450-W CW maximum power is delivered into the pump chamber through slotted windows, providing

uniform pumping to the whole waveguide. The folded hybrid resonator is 215 mm long, comprised by a concave mirror (focal length f =207 mm), a cutaway hard edge output mirror (f =138 mm), and a Brewster angle polarizer (see Fig. 2.13). The magnification of the resonator is 1.5, corresponding to the output loss of 0.33. The resonator equals effectively a case-I/II waveguide resonator in the transverse (guided) direction, and a negative branch confocal unstable resonator in the lateral (unguided) direction. This configuration avoids large inserting losses of the polarizer, typically 5% per pass [3]. The acousto-optical (AO) modulator is 46 mm long and the ultrasonic wave travels in the transverse direction. Mode control in the transverse direction has been achieved by an intracavity aperture just before the output mirror as well as space-waveguide coupling effects from the rear mirror [2].
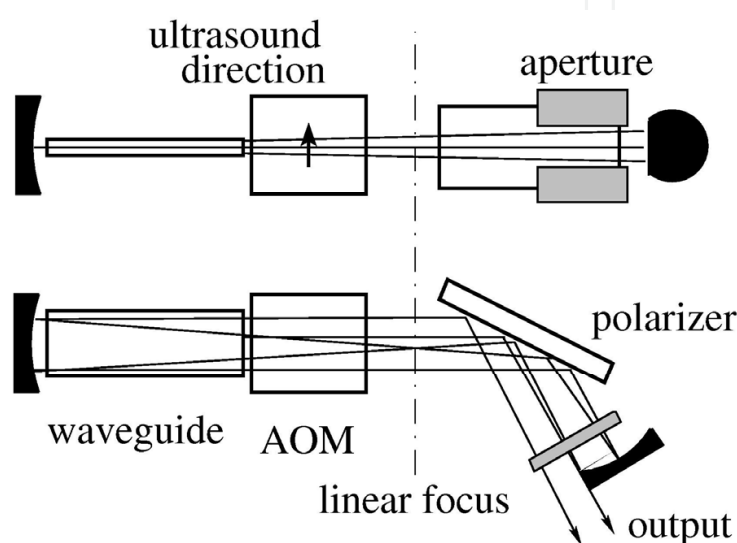

Fig. 2.13. Schematic diagram of the experimental setup.

Planar waveguides can be thought as one dimensional waveguides in the transverse direction and free space propagation in the lateral direction. We assume x- and y-axis are the transverse and lateral directions, respectively. Then, the laser travels along z-axis. The electric field of laser can be expressed as a superposition of the guided modes,

$$E(x,z) = \sum_m E_m(x,z)\exp\{j(\omega t - \beta_m z + \theta_m\}$$ (2.9)

where ω is the angular frequency of the laser electric field; θ_m and β_m are the phase and the propagation constant of the mth order mode, respectively. For the weak-guided waveguide, the propagation constant for the mth order mode can be found approximately as [27]

$$\beta_m = \frac{\omega n}{c} + \frac{m^2 \pi \lambda}{4 n^2 a^2}$$ (2.10)

where n is the refractive index of the core; λ is the laser wavelength in the vacuum; and $a = d + \Delta$ is the effective thickness of the waveguide. Using Δ=5 m for our waveguide, the deviation of (2.10) is less than 0.1% compared with the standard eigen equation. If the origin of x-axis is chosen at the edge of the waveguide, the amplitude of the normalized mth order eigen-mode $E_m(x,z)$ can be written as

$$E(x,z) = A_m(z)\sqrt{\frac{2}{a}}\sin(k_{xm}x) \tag{2.11}$$

where $A_m(z)$ is the amplitude at the origin of x-axis ($x=0$). The x-component of wave vector k_{xm}, the free-space wave vector k, and the propagation constant β_m satisfy $k_{xm} = \sqrt{k^2 - \beta_m^2}$.

Generally, the basic rate equations for Q-switched lasers are described with average photon density. The photon density ϕ is calculated by integrating the electric field over whole space of the waveguide,

$$\phi = \frac{n}{Z_0 Slh\nu}\int_z\int_x E(x,z)E^*(x,z)dxdz \tag{2.12}$$

where Z_0 is the vacuum intrinsic impedance; l and S are the length and cross-sectional area of the waveguide, respectively. $h\nu$ is the photon energy of laser field. Applying the orthogonality of eigen-modes to Eq. (2.12), the total photon density is found to be the sum of photon density of all eigen-modes,

$$\phi = \sum_m \phi_m = \sum_m \frac{n}{Z_0 Sh\nu}\int_z A_m(z)A_m^*(z)dz \tag{2.13}$$

Substituting ϕ from Eq. (2.13) into the standard Q-switched rate equations, we obtain multi-mode rate equations,

$$\frac{d\phi_m}{dt} = \frac{\phi_m}{t_r}(2\sigma Nl - \varepsilon_m) + \phi_{spon}, \quad m = 1, 2, 3 \ldots \tag{2.14a}$$

$$\frac{dN}{dt} = -\gamma\sigma cN\sum_m \phi_m \tag{2.14b}$$

where t_r is the cavity round-trip time; σ the stimulated emission cross-section; N the average population inversion; γ the reduced gain factor [32]; c the speed of light, and ε_m the cavity losses. The contribution of spontaneous emission is taken into account by ϕ_{spon}. Notice that although above equations are derived for TE polarization, they are also valid for TM polarization if the electric field **E** is replaced by the magnetic field **M**. Actually, because our laser worked with TM polarization in the experiments, numerical simulation throughout this chapter has been performed for TM modes.

In the multi-mode rate equations, the cavity losses ε_m are mode dependence. The cavity losses include four parts. They are the output losses $\ln(1/R)$, space-waveguide coupling losses from the rear mirror L_m, losses from the AO modulator $k_m(t)$, and other intrinsic losses O,

$$\varepsilon_m = \ln(1/R) + O + L_m + \kappa_m(t) \tag{2.15}$$

The output losses $\ln(1/R)$ and the intrinsic losses O are almost the same for all modes, but the losses L_m are special for given eigen-modes. These three types of losses are constants

during Q-switching interval. The losses $k_m(t)$ determined by the AO modulator varies with time, playing a important role in the mode competition. The losses $k_m(t)$ can be calculated by wave propagation method. The laser field propagating in the free space is described by the Huygen's integral, [1]

$$E_m(x, z_1) = \int K(x, z_1, z_0) E_m(x, z_0) dx \qquad (2.16)$$

where $K(x, z_1, z_0)$ is the propagation integral kernel [1]. While the laser beam arrives at the AO modulator, the laser beam will be modulated. The radio-frequency (RF) driver power decays exponentially after the AO modulator being triggered. The modulation of the electric field in the AO modulator is given by

$$\tilde{E}(t, x, z_1) = \eta_{AO} \exp\{-(t - x/v)/\tau_{ao}\} E(x, z_1) \qquad (2.17)$$

where η_{AO} is the modulation amplitude of the AO modulator, v is the propagation velocity of ultrasonic wave in silica, and τ_{ao} is the decay constant of the RF driver. The time t is counted from the AO modulator being opened. In our experiments, τ_{ao} was measured to be 100 ns, and the ultrasonic wave spends about 80 ns passing through the laser beam diameter. Thus, the AO modulator can be opened transparently in about 120 ns.

When the laser beam is reflected back to the waveguide, it couples to eigen-modes of the waveguide. For the mth order mode, the coupling coefficient is given by the overlap integral,

$$C_m(t) = \sum_i \sqrt{2/a} \int E_i'(t, x) \exp(j\theta_i') \sin(k_{xm} x) dx \qquad (2.18)$$

where $E_i'(t, x) \exp(j\theta_i')$ is the returned electric field of ith order mode. The contributions to C_m from different eigen-modes are added coherently. The exact value of C_m depends on the relative phase angle among eigen-modes. Finally, the losses $k_m(t)$ is written as

$$k_m(t) = \ln[1 - C_m(t)] \qquad (2.19)$$

If the laser beam propagates in the resonator without disturbance, the contributions to C_m from the ith modes ($i \neq m$) are very small. With an intracavity aperture inserted into the resonator, the electric field is distorted and the contributions from adjacent modes ($i = m \pm 1$) will increase due to the coupling effects among eigen-modes.

At first, we calculate coupling coefficient without the AO modulator in the cavity. If we assume no coupling effects among eigen-modes, the coupling coefficient drops down monotonously with narrowing the intracavity aperture. When the influences from adjacent modes are considered, several ripples, corresponding to constructive interference between eigen-modes, are found in the curves with narrowing the aperture. We compared the coupling coefficient in these two cases in Fig. 2.14. In the figures we assume all modes with the same initial phase and amplitude. As can be seen, the influences of the coupling among eigen-modes are obvious. Notice that TM1 mode has the largest coupling coefficient all the time without the influence of the AO modulator.

Now let us consider the influence of the AO modulator. Because the ultrasonic wave travels from bottom to top in the AO modulator, just after the AO modulator is opened, the mode whose electric field has a side ripple near the bottom of the AO modulator, has the largest transmission in the first instance. While the ultrasonic wave is totally opened, the AO modulator becomes transparent, and then the electric field passes the AO modulator without distortion. The evolution of the coupling coefficient is described in Fig. 2.15. In our experiment, when the intracavity aperture is set to 2-mm wide, a side ripple of TM2 mode locates near the bottom of the AO modulator. Thus, the coupling coefficient of TM2 mode is the largest in the first 120 ns. After that time, TM1 mode obtains the largest coupling coefficient. This time-dependence losses lead to mode competition in the Q-switched planar waveguide lasers. In contrast, the coupling loss is time independent in the CW lasers, and mode competition has not been observed [19].

(a)   (b)
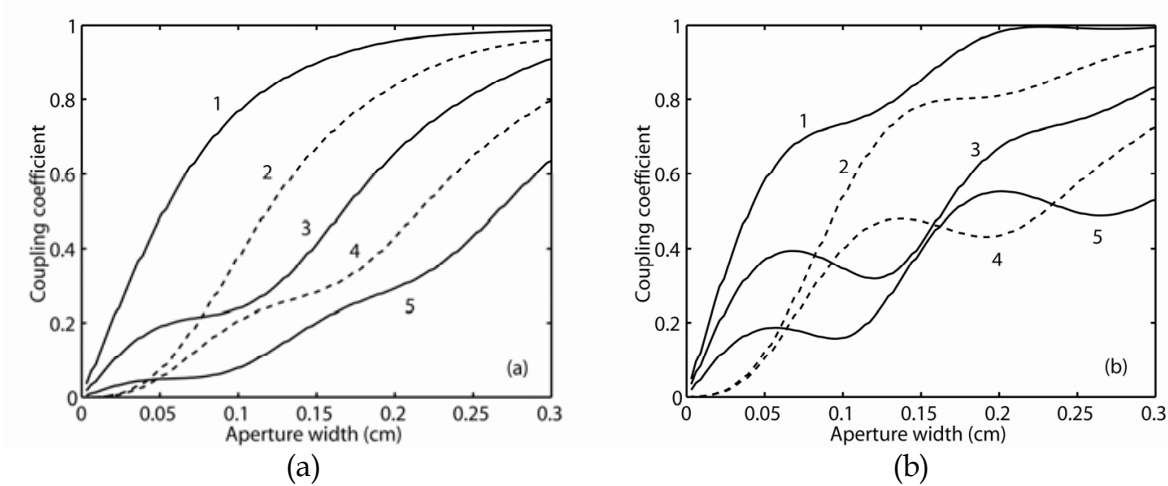
Fig. 2.14. Coupling coefficients of TM1-TM5 modes for varying aperture width without (a) and with (b) mode coupling effects.
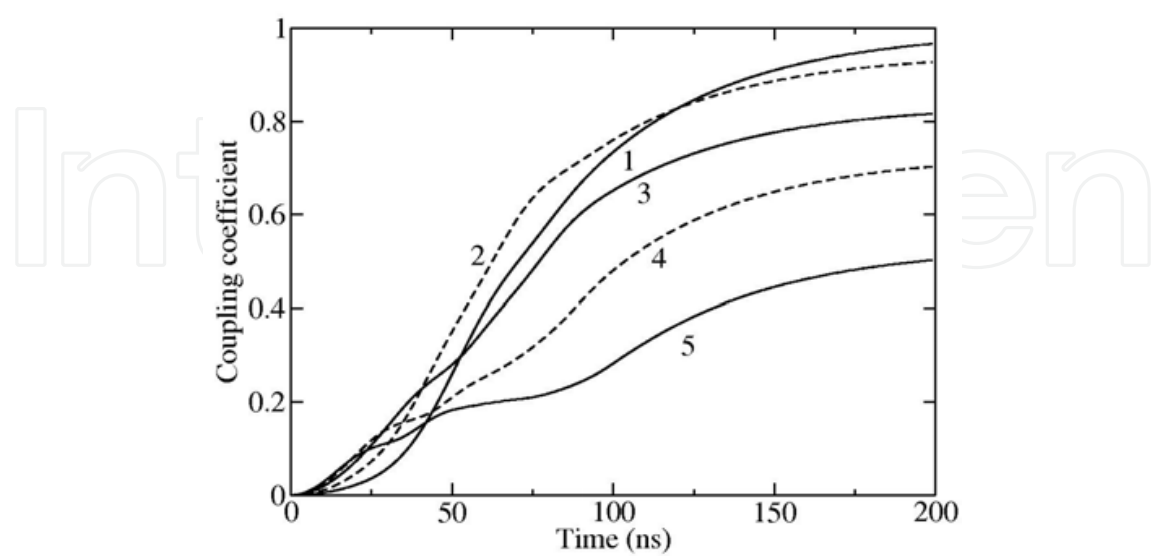

Fig. 2.15. Evolution of coupling coefficients of TM1-TM5 modes after the AO modulator being switched on. The intracavity aperture is 2-mm wide.

In the switch-off interval, population inversion accumulates rapidly under heavy pumping. Parasitic oscillation occurs when its threshold is overcome by the accumulated gain. Then in turn, the parasitic oscillation clamps the population inversion to the level corresponding to the threshold. The parasitic oscillation can be enhanced by the total internal reflection at the waveguide surface along zig-zag path or in-plane path [19]. The parasitic oscillations along different paths deplete particular parts of the population inversion. Therefore, the average population inversion is given by

$$N = \frac{1}{U}\sum_{i=1}^{U} N_i \tag{2.20}$$

The parasitic oscillation propagating along the ith path is governed by the rate equation,

$$\frac{d\Phi_i}{dt} = \Phi_i[c\sigma N_i - \varepsilon_i] + \Phi_{spon} \tag{2.21a}$$

$$\frac{dN_i}{dt} = R_p\eta_p - \frac{N_i}{\tau_2} - c\sigma N_i\Phi_i \tag{2.21b}$$

where ϕ_i, N_i, and ε_i are the photon density, the population inversion and the threshold, respectively. τ_2 is the excited-state lifetime. Pump efficiency is $\eta_p = 0.7$ for our experiments. Pump rate R_p is determined by the pump power.

By measuring the small signal gain, we found the parasitic oscillation occurred when the pump power was around 300 W. Hence, we assume the threshold of the parasitic oscillation corresponding to the pump power of 300 W. The calculated population inversion and photon density of parasitic oscillation are plotted in Fig. 2.16. Without parasitic oscillation [1], the population inversion can be expressed as $R_p\eta_p t[1 - \exp(-t/\tau_2)]$. Comparing this solution with Fig. 2.16, we find the inversion can be several times higher than the parasitic threshold before it is really depleted by the parasitic oscillation. This means that quasi CW pumping sources with short duty-cycles can be beneficial to push the inversion to higher levels. With slow repetition rate, intense pumping is useless because the parasitic oscillation grows so quickly that the inversion has been clamped to the parasitic threshold at the end of pumping interval. For the maximum pump power of 450 W in our experiments, the inversion can be accumulated without severe degradation up to 1-kHz repetition rate.

Once the population inversion at the end of pumping interval having been obtained, we use it as the initial value n_i to the Q-switching equations Eq. (2.14). Solving Eq. (2.14) numerically, we can obtain remaining population inversion n_f at the end of the Q-switched pulse. The remaining inversion n_f is then inserted back into pump equations Eq. (2.20) and (2.21). These procedures have been iterated until the population inversion reaches steady state.

As can be seen from Fig. 2.15, the losses for TM2 mode is less than that of TM1 mode in the first 120 ns. After 120 ns, TM1 mode becomes the one with the lowest loss. With the pump power below 450 W, the build-up time of laser pulse is more than 120 ns, so that single TM1 mode exists during whole pulse duration. When the pump power is increased to 450 W, the

build-up of laser pulse is around 120 ns. TM2 mode can oscillate before 120 ns, but after 120 ns, TM1 mode grows so quickly that TM2 mode is clamped to a low level [see Fig. 2.17(a)]. When the pump power is greater than 450 W, TM2 mode can grow significantly in the first 120 ns. After that time, TM1 mode starts growing. Because the inversion has been saturated down by TM2 mode, finally TM1 mode is lower than TM2 mode [Fig. 2.17(b)].
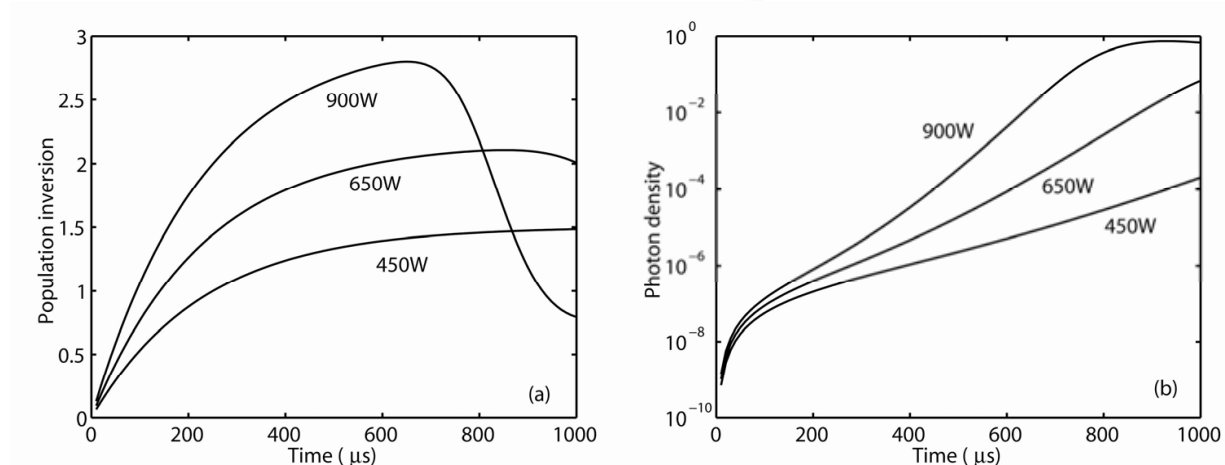

Fig. 2.16. (a) Normalized population inversion, and (b) photon density of parasitic oscillation for various pump powers.
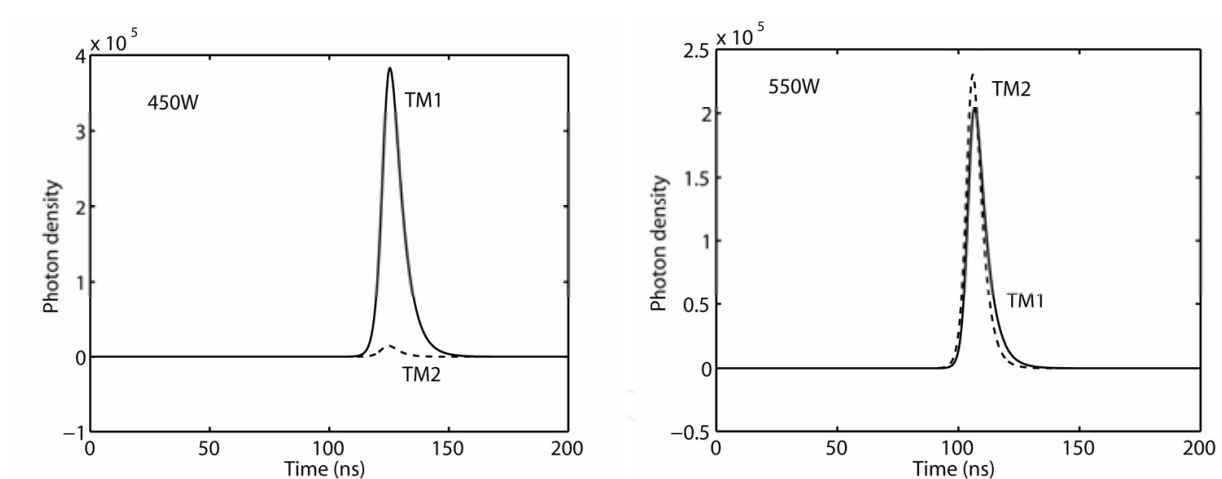
Fig. 2.17. Temporal profiles of TM1 and TM2 modes with pump power of 450 W and 550 W, respectively.

We measured mode structure by scanning the near-field laser beam with a 200-μm-wide slot. The transmission from the slot was recorded with an InGaAs photondetector and an oscilloscope. Then, the mode structure was found by best fitting of measured data to eigen-modes of the waveguide. The results were compared with theoretical simulation in Fig. 2.18. As expected, the percentage of TM2 mode decreases with time. However, in comparison with the simulation, the percentage of TM2 mode is about 8 and 2 times larger with 300 and 450 W pump power, respectively. This may be caused by the thermal distortion in the waveguide, so that the mode controlled by the intracavity aperture is degraded.

Since laser pulses develop from spontaneous emission, pulse instability is a characteristic feature of Q-switched lasers. Because the coupling losses $k_m(t)$ are sensitive to the related phase angle between eigen-modes, the pulse instability in the planar waveguide laser is larger than that in the ones whose output are phase insensitive, e.g., conventional rod lasers. Assuming constant amplitude and random phase of spontaneous emission in the simulation, about 7% fluctuation in the pulse's peak was found. Fig. 2.19 shows a typical pulse train recorded in the experiments for the 450 W pump power and 1 kHz repetition rate.

The fluctuation of the pulse's peak was measured to be about 15%. If we take into account the influence of thermal turbulence and instability of the AO modulator, the measured fluctuation agrees with the simulation. Notice that the mode competition can be suppressed by using the narrower intracavity aperture as doing in CW lasers [19]. In experiments, the pulse fluctuation was reduced to 5% when 1.2-mm wide aperture was used.
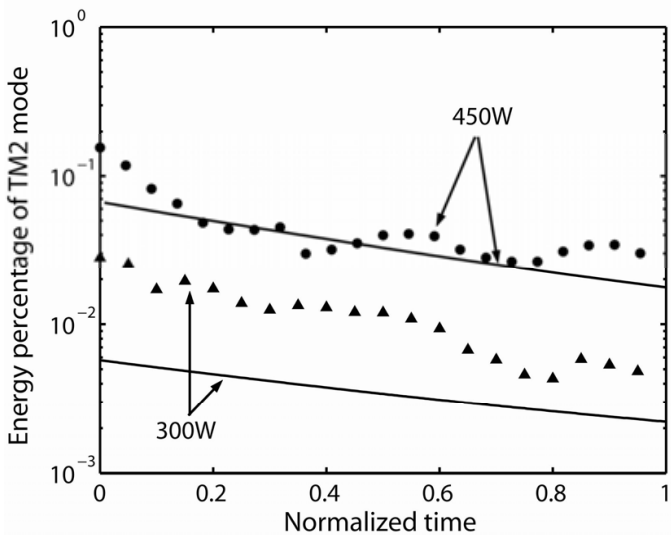

Fig. 2.18. Energy percentage of TM2 mode as a function of normalized time for various pump powers.
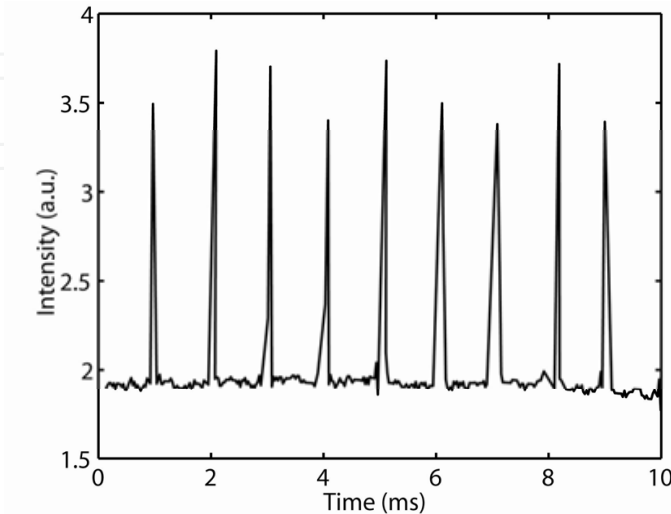

Fig. 2.19. Typical pulse train at 1-kHz repetition rate under 450-W pump power.

As we mentioned previously, the intensity ratio of TM2 mode to TM1 mode depends on the input pump power and varies with time, leading to temporal structures in the output beam patterns. We measured the near-field beam patterns and compared them with theoretical simulation in Fig. 2.20. The near-field beam patterns were recorded at 20 cm far from the output coupler in the pulse rising edge, peak and falling edge, respectively. Under 300 W pump power, because TM1 mode was dominant during whole pulse duration, the output beam pattern was almost invariable. With the pump power increasing to 450 W, TM2 mode was significant in the rising edge, and decreased with time. As can be seen, side ripples were higher in the rising edge than that in the falling edge. The theoretical calculation was obtained by coherent sum of the field of each eigen-modes, because we find that the eigen-modes tend to be phase-locked in the buildup of laser pulses. Further, asymmetry of side ripples is easily explained by the coherent sum. The output beam patterns of planar waveguide lasers vary in a different way from that of rod lasers [33].
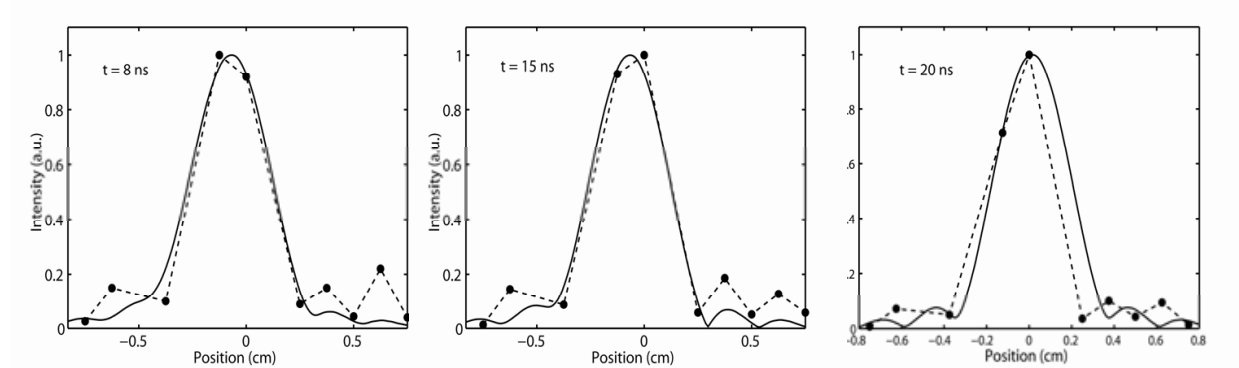

Fig. 2.20. Near-field transverse beam pattern at the rising edge, the peak and the falling edge of the pulse under 450 W pump power. The solid curves are the simulation and the dots are the measured data.
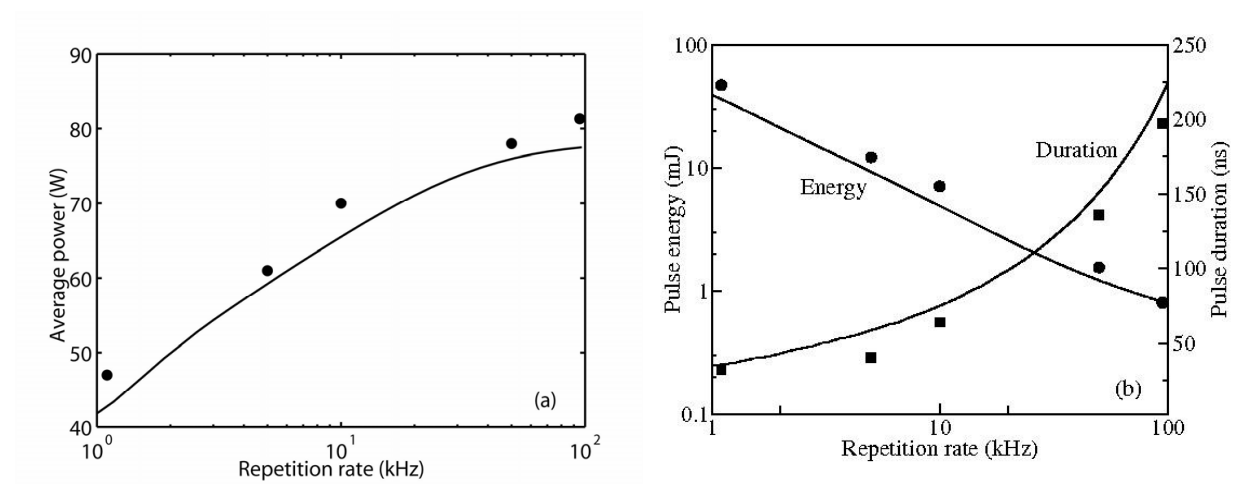

Fig. 2.21. (a) Average power, and (b) pulse energy and duration as a function of repetition rate with 450 W pump power.

The pulse energy was calculated by integrating photon density over whole pulse duration, and the average power was obtained by multiplying the pulse energy with the repetition rate. Bearing pulse instability in mind, we averaged the integration over 20 pulses, where

random phase and amplitude was applied to the spontaneous emission. Accordingly, the data measured in the experiments were averaged over 32 sequential laser pulses. Without intracavity aperture, up to 109 W of average power can be obtained with $M_x^2 \times M_y^2 = 6 \times 1.4$ at 100 kHz repetition rate. Using 2-mm-wide intracavity aperture, a maximum average power of 83 W was generated from the laser with $M_x^2 \times M_y^2 = 1.2 \times 1.4$ at 100 kHz repetition rate. The typical pulse duration and pulse energy at 1 kHz repetition rate were 32 ns and 47 mJ, respectively. Correspondingly, the multi-mode rate equations gives 29 ns pulse duration and 43 mJ pulse energy, compared with 22 ns and 37 mJ using standard single-mode rate equations. The multi-mode model gives a better prediction than that using single-mode assumption.

3. References

[1] A.E. Siegman, *Lasers* (University Science, Maple-Vail, CA, 1986).

[2] H.J. Baker, A.A. Chesworth, D.P. Millas, and D.R. Hall, "A Planar waveguide Nd:YAG laser with a hybrid waveguide-unstable resonator," *Opt. Commun.* 191, 125 (2001).

[3] J. Xu, J.R. Lee, H.J. Baker, and D.R. Hall, "A new Q-switched hybrid resonator configuration for the 100W Nd:YAG planar waveguide laser," presented at CLEO-EURO 2003, Paper CA-2-3-MON, Germany, 2003.

[4] A.E. Siegman, "New development in laser resonators," *Proc. of SPIE* 1224, 2-14 (1990).

[5] E.A. Sziklas, A.E. Siegman, "Mode calculations in unstable resonators with flowing saturable gain. 2: Fast Fourier transform method," *Appl Opt.,* 14, 1874 (1975).

[6] B. Wasilewski, H.J. Baker, and D.R. Hall, "Intracavity beam behavior in hybrid resonator planar-waveguide CO2 lasers," *Appl Opt.,* 39, 6174 (2000).

[7] E.A. Sziklas and A.E. Siegman, "Diffraction calculations using fast fourier transform methods," *Proc of IEEE* 62, 410 (1974).

[8] D.B. Rensch and A.N. Chester, "Iterative diffraction calculations of transverse mode distributions in confocal unstable laser resonators," *Appl Opt.* 27, 997 (1973).

[9] A.N. Chester, "Three-dimensional diffraction calculation of laser resonator modes," *Appl Opt.* 12, 2353 (1973).

[10] T.S. Rutherford, W.M. Tulloch, E.K. Gustafson, and R.L. Byer, "Edge-pumped quasi-three level slab lasers: design and power scaling," *IEEE J. Quantum Electron.* 36, 205 (2000).

[11] Z. Wang, X. Ye, T. Fang, J. Xu, "Output beam quality of edge pumped planar waveguide lasers with confocal unstable resonators," Optical Review, 12, 391 (2005)

[12] R. Ulrich and G. Ankele, "Self-imaging in homogeneous planar optical waveguides," *Appl. Phys. Lett.* 27, 337 (1975).

[13] J. Xu, "Quasi self-image planar waveguide lasers with high-power single-mode output," *Opt. Commun.* 259, 251 (2006).

[14] H.J. Baker, J.R. Lee, and D.R. Hall, "Self-imaging and high-beam-quality operation in multi-mode planar waveguide optical amplifiers," *Optics Express* 10, 297(2002).

[15] J.Banerji, A.R. Davies, and R.M. Jenkins, "Laser resonators with self-imaging waveguides," *J. Opt. Osc. Am.* B 14, 2378 (1997).

[16] I.T. McHinnie, J.E. Koroshetz, W.S. Pelouch, D.D. Smith, J.R. Unternahrer, and S.W. Henderson, "Self-imaging waveguide Nd:YAG laser with 58% slope efficiency," presented at CLEO/QELS 2002, USA, 262(2002).

[17] W. Koechner, *Solid-state laser engineering* (Spring-Verlag, Berlin, 1999).

[18] J.I. Mackenzie, and D.P. Shepherd, "End-pumped, passively Q-switched Yb:YAG double clad waveguide laser," *Opt. Lett.* 27, 2161 (2002).

[19] J.R. Lee, H.J. Baker, G.J. Friel, G.J. Hilton, and D.R. Hall, "High-average-power Nd:YAG planar waveguide laser that is face pumped by 10 laser diode bars," *Opt. Lett.* 27, 524 (2002).

[20] J.M. Eggleston, T.J. Kane, K. Kuhn, J. Unternahrer, and R.L. Byer, "The slab geometry laser - part I: Theory," *IEEE J. Quantum Electron.* QE-20, 289 (1984).

[21] D. C. Brown, "Nonlinear thermal and stress effects and scaling behavior of YAG slab amplifiers," *IEEE J. Quantum Electron.* 34, 2393 (1998).

[22] D.P. Shepherd, S.J. Hettrick, C. Li, J.I. Mackenzie, R.J. Beach, S.C. Mitchell and H.E. Meissner, "High-power planar dielectirc waveguide lasers," *J. phys. D: Appl. Phys.* 34, 2420 (2001).

[23] A. Faulstich, H.J. Baker and D.R. Hall, "Face pumping of thin, solid-state slab lasers with laser diodes," *Opt. Lett.* 21, 594 (1996).

[24] C. Becker, T. Oesselke, J. Pandavenes, R. Ricken, K. Rochhausen, G. Schreiber, W. Sohler, H. Suche, R. Wessel, S. Balsamo, I. Montrosset and D. Sciancalepore, "Advanced Ti:Er:LiNbO3 Waveguide Lasers," *IEEE J. Selected Topics in Quantum Electron.* 6, 101 (2000).

[25] J. Xu, and Q. Lou, "Gain-guide effects in transient Raman amplifiers," *J. Opt. Soc. Am.* B 16, 961 (1999).

[26] Ling Xiao, Xiaojin Cheng, and Jianqiu Xu, "High-power Nd:YAG planar waveguide laser with YAG and Al_2O_3 claddings", Optics Comm. 281, 3781(2008)J. Xu, H.J. Baker, D.R. Hall, "Mode competition in acousto-optically Q-switched planar waveguide lasers," *Optics and Laser Technology*, 39, 814 (2007)

[27] J. Xu, H.J. Baker, D.R. Hall, "Mode competition in acousto-optically Q-switched planar waveguide lasers," Optics and Laser Technology, 39, 814 (2007)

[28] N. P. Barnes, "Solid-state lasers from an efficiency perspective," *IEEE J. Selected Topics in Quantum Electron.* 13, 435 (2007).

[29] N. Hodgson, V.V. Ter-Mikirtychev, H.J. Hoffman, W. Jordan, "Diode-pumped, 220W ultra-thin slab Nd:YAG laser with near-diffraction limited beam quality," in Advanced Solid-State Lasers, OSA TOPS, 68, 552 (2002).

[30] J.J. Degnan, "Optimization of passively Q-switched lasers," *IEEE J. Quantum Electron.* 31, 1890 (1995).

[31] J. Dong, J. Lu and K. Ueda, "Experiments and numerical simulation of a diode-laser-pumped Cr, Nd:YAG self-Q-switched laser," *J. Opt. Soc. Am.* B 21, 2130 (2004).

[32] J. J. Degnan, "Theory of the optimally coupled Q-switched Laser," *IEEE J. Quantum Electron.* 25, 214 (1989).

[33] A. Caprara and G. C. Reali, "Time varing M^2 in Q-switched lasers," *Opt. and Quantum Electron.* 24, S1001 (1992).
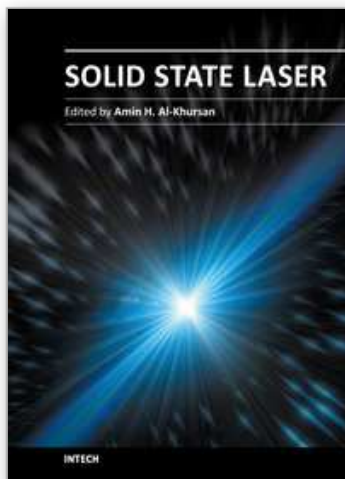
Solid State Laser

Edited by Prof. Amin Al-Khursan

This book deals with theoretical and experimental aspects of solid-state lasers, including optimum waveguide design of end pumped and diode pumped lasers. Nonlinearity, including the nonlinear conversion, up frequency conversion and chirped pulse oscillators are discussed. Some new rare-earth-doped lasers, including double borate and halide crystals, and feedback in quantum dot semiconductor nanostructures are included.

How to reference

In order to correctly reference this scholarly work, feel free to copy and paste the following:

Jianqiu Xu (2012). Diode Pumped Planar Waveguide/Thin Slab Solid-State Lasers, Solid State Laser, Prof. Amin Al-Khursan (Ed.), ISBN: 978-953-51-0086-7, InTech, Available from: http://www.intechopen.com/books/solid-state-laser/diode-pumped-planar-waveguide-thin-slab-solid-state-lasers